International Tables for Crystallography (2018). Vol. H, Chapter 2.8, pp. 174–188.

2.8. Powder diffraction in external electric and magnetic fields

H. Ehrenberg, M. Hinterstein, A. Senyshyn and H. Fuess

2.8.1. Introduction

The functionality of materials depends strongly on the crystalline structure and structural changes during operation. The term 'structure' usually refers to the ideal structure, which specifies the positions of the atoms in a lattice, and thus the distances and angles between them. This idealized model is, however, far too simple to describe the full functionality of a material in a device. Many types of defects, such as point defects, dislocations or grain boundaries, are essential to the functionality and have to be taken into account. As the length scales of defects range from atomic bond lengths *via* nanometres to micrometres, different methods have to be used for comprehensive structural characterization. High-resolution transmission electron microscopy (HRTEM) is the ideal tool for studying a material at the atomic scale, as it gives direct evidence of the arrangement of atoms. In addition, information on the chemical composition can be provided through X-ray or electron spectroscopies. However, in many cases electron microscopy requires a tremendous effort in sample preparation. Furthermore, the application of electric fields in a TEM column is a serious challenge with significant limitations. While electron microscopy will provide information on small sample volumes, diffraction methods probe larger quantities of samples, but give average information. In general, diffraction methods are based on electromagnetic or particle waves. X-ray photons with energies in the keV range have wavelengths similar to interatomic distances and, therefore, X-rays from laboratory sources or synchrotrons are the most widely used. Thermal neutrons with meV energies have complementary properties suited for other applications. While electrons are usually used for microscopy techniques, the field of electron crystallography has developed in recent years. However, given the very small size of an electron beam, its short wavelength (*circa* 0.03 Å) and high absorption, most particles studied by electron crystallography can be considered as single crystals. The combination of electron crystallography and powder diffraction is a powerful tool for tiny crystalline samples, especially inclusions (Weirich *et al.*, 2006).

In the field of *in situ* materials research, multiparametric measurements as functions of three or more external parameters, *e.g.* temperature–magnetic field–pressure or temperature–magnetic field–electric field, have been reported. However, the majority of so-called *in situ* studies are carried out as a function of temperature and sometimes of external pressure. Studies of structural changes under electric fields are relatively rare. Studies of changes due to magnetic fields almost entirely lie in the domain of neutron scattering, where single-crystal experiments usually give more details on the evolution of the magnetic structure. The challenges, necessary instrumentation and some examples of *in situ* diffraction measurements are described in Chapter 16 of the book *Modern Diffraction Methods* (Mittemeijer & Welzel, 2012).

2.8.2. Experimental conditions

Several challenges have to be overcome for experiments under external fields, so the exerimental conditions have to be adapted accordingly. As all these experiments are based on time-dependent conditions, the first requirement is a detecting system that allows fast data acquisition. Considerable progress in recent years has made time resolution of the order of nanoseconds possible (Schmitt *et al.*, 2007), thus enabling stroboscopic diffraction experiments. Higher time resolutions are possible with careful synchronization of the experiment with the time structure of a synchrotron X-ray beam. The electron bunches in a synchrotron are usually separated by several tens to hundreds of nanoseconds and have a width in the range of picoseconds. Once the gating window of an experiment is smaller than the time between successive bunches, the time resolution immediately reaches the width of a bunch. Structural responses to external stimuli are related to displacements of atoms and changes in unit-cell distortion (*i.e.* lattice parameters). The displacements are fairly small and thus very high sensitivity is a prerequisite. In order to study small unit-cell distortions, very good angular resolution is mandatory. The potential angular resolution that is possible in synchrotron experiments is very often not reached for powder samples, as the half-widths of the reflections are mainly determined by the microstructure.

In monochromatic neutron diffraction, the greater divergence of a neutron beam compared to a synchrotron beam and its spectral width ($\Delta\lambda/\lambda$) usually only allow a resolution in the range $\Delta d/d \simeq 10^{-2}$ to be achieved with medium-resolution (high-intensity) diffractometers; this can be tuned down to $\Delta d/d \simeq 10^{-3}$ by tightening the beam collimation at high-resolution monochromatic instruments. Significantly better resolution of $\Delta d/d \simeq 4 \times 10^{-4}$ can be achieved by combining the neutron time-of-flight technique with long neutron flight paths (*circa* 100 m) in back-scattering geometry. Even higher $\Delta d/d$ values (potentially down to 10^{-6}) can be obtained using the spin-echo-based neutron-scattering technique called Larmor diffraction (Repper *et al.*, 2009). The advantages of neutrons over X-rays are that they penetrate more deeply through materials, their scattering form factors are nearly independent of momentum transfer, and they are sensitive to the isotopic composition of a material, enabling accurate location of light elements in the presence of heavy ones, as well as the ability to distinguish between neighbouring elements in the periodic table. Whereas both synchrotron radiation and neutron scattering may be used to elucidate crystal structures under an electric field, neutrons can also be used to study magnetic order and its modification under a magnetic field. Therefore, the examples listed here for studies under electric fields use both kinds of radiation, whereas the examples of studies involving magnetic fields mainly use neutron scattering.

The properties of the materials discussed in this chapter are intimately related to their crystal structures; hence, any change in crystal structure is immediately reflected in the properties. The examples we have chosen are dominated by ferroelectric ceramics and lithium-ion battery materials on the one hand and multiferroic materials on the other.

Most reports in the literature on *in situ* or *in operando* studies deal either with the kinetics of chemical reactions (intercalation, crystallization, catalysis) or structural changes of materials under varying external conditions (temperature, pressure *etc.*). This

chapter is devoted to structural modifications under external fields, both electric and magnetic. The application of external fields requires dedicated sample environments; these often result in an increase in absorption and contribute to the scattering. Furthermore, some components of the devices used for these studies can cause inhomogeneity in the sample or texture. Challenges can be presented by, for example, the deposition of metallic contacts on ferroelectric ceramics, the pronounced materials interaction and mass transport accompanied by changes in electrode volumes in Li-ion batteries, and the housing of magnets.

2.8.2.1. *Detectors*

For an *in situ* or *in operando* study, the choice of detector depends on the specific demands of the study with respect to angular resolution and speed of data collection. High angular resolution is needed to investigate small changes in reflection profiles, resulting from tiny modifications in the microstructure. Fast data collection is generally desirable, but is particularly important when monitoring metastable states in fast and irreversible processes. For a general overview of commonly used X-ray detector systems see Chapter 2.1. The following is a detailed overview of detector systems with high angular or time resolution for X-ray as well as neutron powder diffraction.

For synchrotron X-ray diffraction, analyser crystals between the sample and detector allow angular resolutions to be achieved at the physical limit. Detection is performed point by point, or with a set of point detectors in a multi-analyser crystal detector (MAD) (Toraya *et al.*, 1996; Hodeau *et al.*, 1998; Lee *et al.*, 2008; Peral *et al.*, 2011). The angular resolution of these detectors is only limited by the Darwin width of the analyser crystals, the energy bandwidth of the monochromator and the divergence of the incoming beam.

Gas counters or neutron scintillators are usually used for the detection of thermal neutrons. Because of the shortage of ^{3}He for research applications, alternative technologies are undergoing rapid development, including ^{10}B-based detectors such as Cascade (Köhli *et al.*, 2016), Jalousie (Stefanescu *et al.*, 2017) and Multigrid (Anastasopoulos *et al.*, 2017). However, owing to their relatively low efficiency for thermal neutrons compared with ^{3}He gas counters, neutron detectors that involve ^{10}B(n,α)^{7}Li conversion are mainly used for neutron non-diffraction applications. Even though an analyser setup would in theory be possible for neutron diffraction experiments, the drastically increased time that would be required for data acquisition means that it is not feasible. Alternative concepts have evolved for the use of monochromatic neutrons in powder diffraction with high angular resolution. Multidetectors consist of 80 (SPODI, Hoelzel *et al.*, 2007) or 128 (ECHIDNA, Liss *et al.*, 2006; D2B, Suard & Hewat, 2001) detection units [1/3, 1/2 or 1 inch (where 1 inch = 2.54 cm) diameter ^{3}He tubes, either position-sensitive or not] separated by a small angle and with Soller collimators installed in front. This requires a stepwise re-positioning of the detector bank in order to collect data for complete patterns. The angular resolution of these instruments is limited by the beam divergence, the energy bandwidth of the monochromator and grain-size effects (Liss *et al.*, 2006). A reduction in the divergence of a neutron beam is associated with a considerable loss of intensity. The prerequisites of low divergence and high take-off angle of the monochromator have to be optimized in combination with a two-dimensional detector system. The height of the detectors is limited, however, by the 'umbrella' effect, which produces a broadening of the Debye–Scherrer rings. This effect may be partially compensated for during the numerical data-reduction process (Hoelzel *et al.*, 2012). On the other hand, the detection of some extended sections of the Debye–Scherrer rings provides additional information on strain and texturing.

For a compromise of high angular resolution and fast data acquisition, one-dimensional strip detectors have become popular. These detectors allow data collection in one shot and thus no re-positioning is required. However, if more than one module is used, the gaps between the modules have to be filled by measuring two different positions. Silicon microstrip sensors are used for detecting X-rays (Bergamaschi *et al.*, 2009). The MYTHEN II detector system consists of a set of modules, each consisting of 1280 50 µm-pitch strips, which are wirebonded to the photon-counting readout (Bergamaschi *et al.*, 2009). In combination with a set of vertically focusing mirrors and a sagittally focusing second monochromator crystal, high angular resolution can be achieved together with short acquisition times (for example at the materials science beamline X04SA at the Swiss Light Source) (Patterson *et al.*, 2005). In order to cope with instantaneous many-photon deposition, which is typical of X-ray free-electron lasers (XFELs), a similar system based on the charge-integration principle has been developed (GOTTHARD, Cartier *et al.*, 2014).

For detecting neutrons, microstrip detectors are used, which consist of thin-film metallic strips of anodes and cathodes, deposited on electrically conducting Fe-containing 'black' glass in a ^{3}He gas chamber (*e.g.* D20, Hansen *et al.*, 2008). Similar specifications can be realized with a multiwire setup in ^{3}He gas chambers (WOMBAT, Studer *et al.*, 2006). The multiwire detector has the advantage of being fully two-dimensionally sensitive. This allows for a larger aperture along the wires. The angular resolution can be maintained in the data-reduction process through straightening of the Debye–Scherrer rings. As Soller collimators cannot be used in front of a multiwire or multistrip detector, the effects of sample environments are eliminated by radial oscillating collimators. Multiwire and multistrip detectors are usually installed at high-throughput instruments, whereas high-resolution powder diffractometers are equipped with multidetector systems.

In materials science the investigation of real structure effects can be important. These can include texturing, where the orientation of the sample with respect to the scattering vector is crucial, or diffuse scattering in crystalline materials, and where a large dynamic intensity range has to be covered. The most efficient way of detecting these effects is to use two-dimensional detectors. In most cases the detector is mounted on a set of translational stages, so that the setup can be optimized for either high angular resolution or a wide angular range (Herklotz *et al.*, 2013).

When high-energy X-rays are used, two-dimensional detectors based on digital flat-panel technology are the best choice. They combine an amorphous Si panel with a CsI:Tl or various Gd_2O_2S:Tb scintillators. Pixel sizes of 200 × 200 µm (Perkin Elmer 1621N ES, Herklotz *et al.*, 2013) or 154 × 154 µm (Pixium 4700, Daniels & Drakopoulos, 2009) together with frame rates of up to 60 frames per second overcome several drawbacks of the high-energy detectors that were previously available.

For soft X-rays a range of two-dimensional detectors has been developed. The PILATUS detector (Kraft *et al.*, 2009) is a silicon-based hybrid pixel detector system, similar to the MYTHEN strip detector. Instead of a one-dimensional strip setup, individual modules with 487 × 195 pixels of identical pitch (172 × 172 µm)

are combined into a detector array of up to 6 224 001 pixels. A further development of the PILATUS detector is the EIGER detector (Johnson *et al.*, 2014). The system consists of single-photon-counting modules of 256 × 256 pixels with a significantly reduced pitch of only 75 × 75 μm. Like GOTTHARD, the charge-integrating equivalent of MYTHEN, the JUNGFRAU detector (Mozzanica *et al.*, 2014) was developed as a charge-integrating equivalent to the PILATUS and EIGER detectors.

Even smaller pixel sizes of 55 × 55 μm have been achieved for the hybrid pixel detector Medipix3 (Ballabriga *et al.*, 2007). Modules of 256 × 256 pixels can be combined into large arrays. The electronics are highly configurable and allow charge summing, programmable binary counter and continuous count–read modes.

In principle, fast data collection seems to be desirable, but it has to be adjusted to the process that is being investigated. In most cases for a continuous frame rate the limiting factor is the data rate. The MYTHEN II detector (Schmitt *et al.*, 2003) installed at the Swiss Light Source allows a frame rate of 10–90 Hz, depending on the desired dynamic range (24–4 bits), and thus observations in the time range below 1 s to 10 ms. The two-dimensional detectors for high-energy X-rays can operate at a maximum of 30 Hz (Perkin Elmer) or 60 Hz (Pixium). In this context it is also worth mentioning the PILATUS detectors – a series of silicon pixel detectors also developed at the Swiss Light Source and further commercialized by Dectris. These detectors possess a high dynamic range over five orders of magnitude along with a rate capability of $>2 \times 10^6$ photons s^{-1} $pixel^{-1}$ and excellent detection efficiency of nearly single-photon counting (99% at 8 keV and 55% at 15 keV). The use of 1000 μm-thick CdTe instead of silicon enables >90% quantum efficiency at 20 keV, 81% at 40 keV, 90% at 60 keV, 77% at 80 keV and 56% at 100 keV. Complex detectors are often characterized by a long readout time of a large number of two-dimensional pixels, *e.g.* for PILATUS detectors the readout time per module is ∼2.7 ms.

Semiconductor-based detectors can operate at significantly higher frame rates. The EIGER detector can operate at a maximum frame rate of 24 kHz, while GOTTHARD can reach 40 kHz. In a special burst mode of 128 frames, a frame rate of 800 kHz is possible, reaching a single exposure time of 1.25 μs. The Timepix3 detector (Poikela *et al.*, 2014), which is a further development of the Medipix3 detector, can theoretically sustain continuous frame rates of up to 200 kHz, as long as the overall hit rate is less than 80 MHz.

In order to collect enough intensity for fast processes or to investigate even shorter timescales, stroboscopic measurements are useful. Thus, timescales in the range of milliseconds down to nanoseconds may be followed using a pump–probe setup. In this technique, the reaction is first triggered (pump) and after a specific time delay the diffraction pattern is collected (probed). The use of rapidly rotating choppers in the incoming beam is an attractive alternative to pump–probe experiments (Yoo *et al.*, 2011). Time resolution in the microsecond regime is routinely obtained in synchrotron experiments (Hinterstein, 2011; Hinterstein *et al.*, 2014) and in about the millisecond regime in neutron diffraction (Eckold *et al.*, 2010). When these experiments are conducted at a synchrotron and the periodic excitation of the sample is synchronized with the bunch clock of the synchrotron, the time resolution can be increased significantly. For a time resolution smaller than the temporal separation of the particle bunches (typically 8–200 ns), the time resolution suddenly drops to the bunch width, which is in the range of picoseconds. For neutron diffraction, the limiting factor for time resolution can be calculated from the energy bandwidth and the speed of the neutrons, which is dependent on the wavelength. The lower limit is typically in the range of 25 μs. These time ranges can be reached by multistrip or multiwire detectors in a stroboscopic setup.

In situ and *in operando* measurements require a specific sample environment, which is normally built using a different material to the sample and leads to additional contributions to the diffraction pattern. The use of strongly scattering materials such as thin metallic foils (Al foil in batteries, Ag or Au films as electrodes) or single crystals (sapphire capillaries for high-temperature experiments or diamonds in high-pressure experiments) may seriously bias data collection or damage the detector. If it is not possible to eliminate them by masking, they have to be taken into account by Rietveld analysis or profile matching. A correct treatment of the contributions from the sample environment has to take into consideration the fact that the additional scattering is normally off the diffractometer centre and this sample shift produces a non-linear shift in 2θ of the corresponding reflections in the pattern.

2.8.2.2. *Absorption*

Additional equipment is required for *in situ* experiments. The necessary parts are quite often constructed from metallic components. Light metals like aluminium are preferred for shielding parts within the beam for neutrons and X-rays. Vanadium is a suitable choice in neutron experiments, as it has a very small scattering cross section, so produces almost no coherent scattering. In most cases a suitable absorption correction is mandatory. For X-rays the energy dependence of the linear absorption coefficient $\mu(E)$ is very pronounced, especially close to X-ray absorption edges. Away from an absorption edge, higher energies lead to lower absorption. As an example, the linear absorption coefficient μ for steel (α-Fe) at 45 keV is 0.18 cm^{-1} and at 60 keV it is 0.076 cm^{-1}. The transmitted intensity after a beam has penetrated 1 mm steel with 100% packing density twice (once for the incoming and once for the outgoing beam) is therefore 2.7% for 45 keV but 22% for 60 keV. For one of the examples treated later, the piezoceramic $Pb(Zr_{0.5}Ti_{0.5})O_3$, the calculation for a sample diameter of 1 mm and a typical packing density of 60% in a powder leads to beam transmission of 3% (45 keV) and 21% (60 keV). Therefore, using high-energy X-rays enables transmission diffraction experiments that are not feasible with lower energies. The gain in measured intensities by decreasing absorption normally overcompensates for the decrease in scattering at shorter wavelengths, which is proportional to λ^3 within kinematical theory. The linear absorption coefficient of thermal neutrons (with wavelengths from 1 to about 3 Å) is small for most elements and scales in proportion to the wavelength, $\lambda = h/p = h/(2mE)^{1/2}$, *i.e.* λ (Å) = $9.045/E^{1/2}$ (meV) = $3956/v$ (m s^{-1}). However, the absorption cross sections for different isotopes of the same element may be very different. Numerical values are listed in Sears (1992) and *International Tables for Crystallography* Volume C, Table 4.4.4.1. For ferroelectric $Pb(Zr_{0.5}Ti_{0.5})O_3$, the linear neutron absorption coefficient at a wavelength λ = 1.5 Å and for a packing density of 60% is 0.026 cm^{-1}, significantly smaller than for X-rays; it is mainly determined by the Ti content.

As both the scattering and the absorption cross section for neutrons are in most cases much smaller than for X-rays, bigger samples are required. On the one hand, this leads to the advantage of better averaging over many particles. On the other hand,

the spatial resolution is significantly affected by the sample dimensions because of self-collimation. The appropriate choice of diffraction method is defined by the particular scientific challenge and has to take into consideration the different amount of sample that is needed for each experiment.

Very high absorption cross sections are desirable for shielding purposes. In X-ray diffraction, lead or tungsten are widely used. Only a few isotopes have a nuclear resonance in the thermal neutron range and thus a high absorption cross section. The most prominent are ^{10}B, ^{113}Cd and ^{157}Gd, which are used in neutron optics as collimators, attenuators and beam-shaping devices.

2.8.2.3. *Sample fluorescence and incoherent neutron scattering*

Sample fluorescence is a common problem for laboratory X-ray powder diffractometers, which are neither equipped with an analyser nor use detectors with a narrow energy resolution. In powder diffraction using synchrotron radiation, this problem is often solved either by adjusting the energy of the incident beam or by an adjustment of the dynamic range of the detector, or by a combination of both.

Like absorption cross sections, the incoherent neutron scattering lengths for different elements and isotopes do not vary in any obviously systematic way throughout the periodic table. Among the known stable isotopes, ^{1}H has the largest incoherent scattering length (25.274 fm) and has a small and negative coherent one (−3.7406 fm). The situation is very different for ^{2}H (deuterium), for which the incoherent and coherent scattering lengths are 4.04 and 6.671 fm, respectively. Differences between the coherent scattering lengths of hydrogen and deuterium form the basis of the isotopic labelling technique, called contrast matching; this is particularly important in applications of neutron scattering to hydrogen storage, structural biology and polymer science. Deuteration of samples is a challenging task, but obtaining high-quality powder diffraction data from hydrogenated samples is far more difficult. Use of neutron polarization analysis is a reliable way to subtract the incoherent scattering contribution from the diffraction data (Mikhailova *et al.*, 2012), but it is often accompanied by significant losses of incident neutron flux and, consequently, of data quality. Both sample fluorescence and incoherent neutron scattering are isotropic and, therefore, are often considered as a background in powder diffraction experiments.

2.8.3. Examples

2.8.3.1. *In situ studies of ferroelectrics in an external electric field*

The function of ferroelectrics as stress sensors, high-frequency microphones, medical injectors or large strain actuators is based on electric poling. A polycrystalline material exhibits a zero net polarization. When an electric field is applied to the sample, the spontaneous electric polarization of the ferroelectric material is reoriented along the electric field vector. This occurs by a reorientation of domains. Additional polarization is obtained by an increase of the spontaneous polarization induced by the applied electric field. With *in situ* experiments, the field-induced changes in the powder diffraction reflections are measured. Fig. 2.8.1 is a schematic representation of some *in situ* sample geometries. The electric field is applied *via* electrodes on the sample surface.

Many of these ferroelectric materials crystallize in a structure derived from the cubic perovskite type, but in a crystal system with lower symmetry and with a non-centrosymmetric space group. The most widely used material is lead zirconate-titanate ($PbZr_{1-x}Ti_xO_3$, PZT), which exhibits the highest strain response

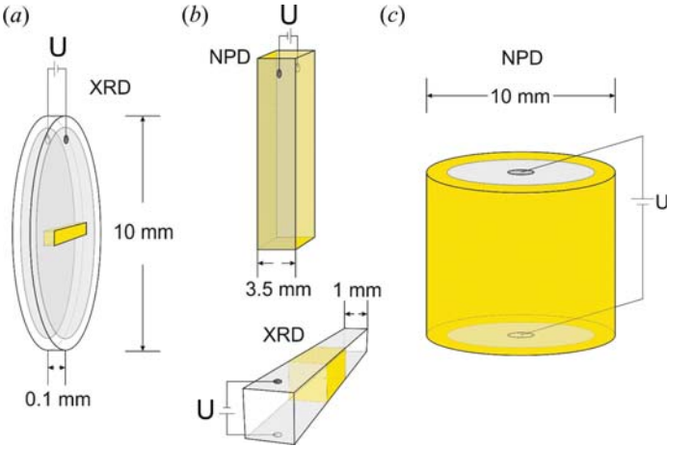

Figure 2.8.1
Sample geometries for *in situ* experiments with an applied electric field. Samples are poled *via* an applied voltage (U) at the sample electrodes (grey). Different sample geometries are necessary to account for different beam sizes, absorption and detector concepts. Yellow indicates the irradiated sample volume. (*a*) Flat-plate samples for X-ray experiments with strip detectors, limiting photon energies to around 30 keV. (*b*) Bar-shaped samples for high-intensity neutron powder diffraction (NPD) or high-energy X-ray diffraction (XRD). (*c*) Cylinder-shaped samples for high-resolution neutron diffraction with fixed detector collimators.

at the so-called morphotropic phase boundary with a composition of about 50% for Ti and Zr. It is generally accepted that the phase on the Ti-rich side of the PZT phase diagram has a tetragonal structure with space group *P*4*mm*. On the rhombohedral Zr-rich side, two ferroelectric phases can be identified, with space groups *R*3*m* for high and *R*3*c* for low temperatures. A considerable amount of work has been devoted to the elucidation of the crystal structure of the material close to the morphotropic phase boundary. Neutron and synchrotron diffraction detected monoclinic symmetry at low temperatures and nanometre-sized regions (the so-called polar nanoregions) were inferred from diffuse scattering (Noheda *et al.*, 2000; Hirota *et al.*, 2006). Alternative interpretations explained the new reflection found in the pattern between the 111_C and 200_C reflections (where the subscript 'C' corresponds to the cubic archetype structure) as diffuse scattering from diffuse incoherent scattering by small domains (Jin *et al.*, 2003).

Unique information on structural changes during poling is obtained from *in situ* studies in applied external electric fields (Hoffmann *et al.*, 2001). Fig. 2.8.2 displays two groups of powder reflections (Schönau, Schmitt *et al.*, 2007) observed by synchrotron X-ray diffraction. They are directly compared with the domain structure from TEM observations (Schmitt *et al.*, 2007) for a range of compositions near the morphotropic phase boundary. One group of reflections is derived from the cubic 111_C reflection, the other from the archetype 200_C reflection. The transition from the rhombohedral splitting to the tetragonal one with increasing Zr content is correlated with the forms of ferroelectric domains in TEM. Close to the morphotropic phase boundary, nanodomains (ranging in width from 20 to 200 nm) are observed in addition to the well known microdomains. The nanodomains react immediately under the influence of an electric field to become microdomains. Fig. 2.8.3 shows the intensity changes observed for the 110_C group of reflections. The changes under an electric field are pronounced and depend on the *c*/*a* ratio (Schönau, Knapp *et al.*, 2007), the formation and disappearance of nanodomains, and the local symmetry of these domains.

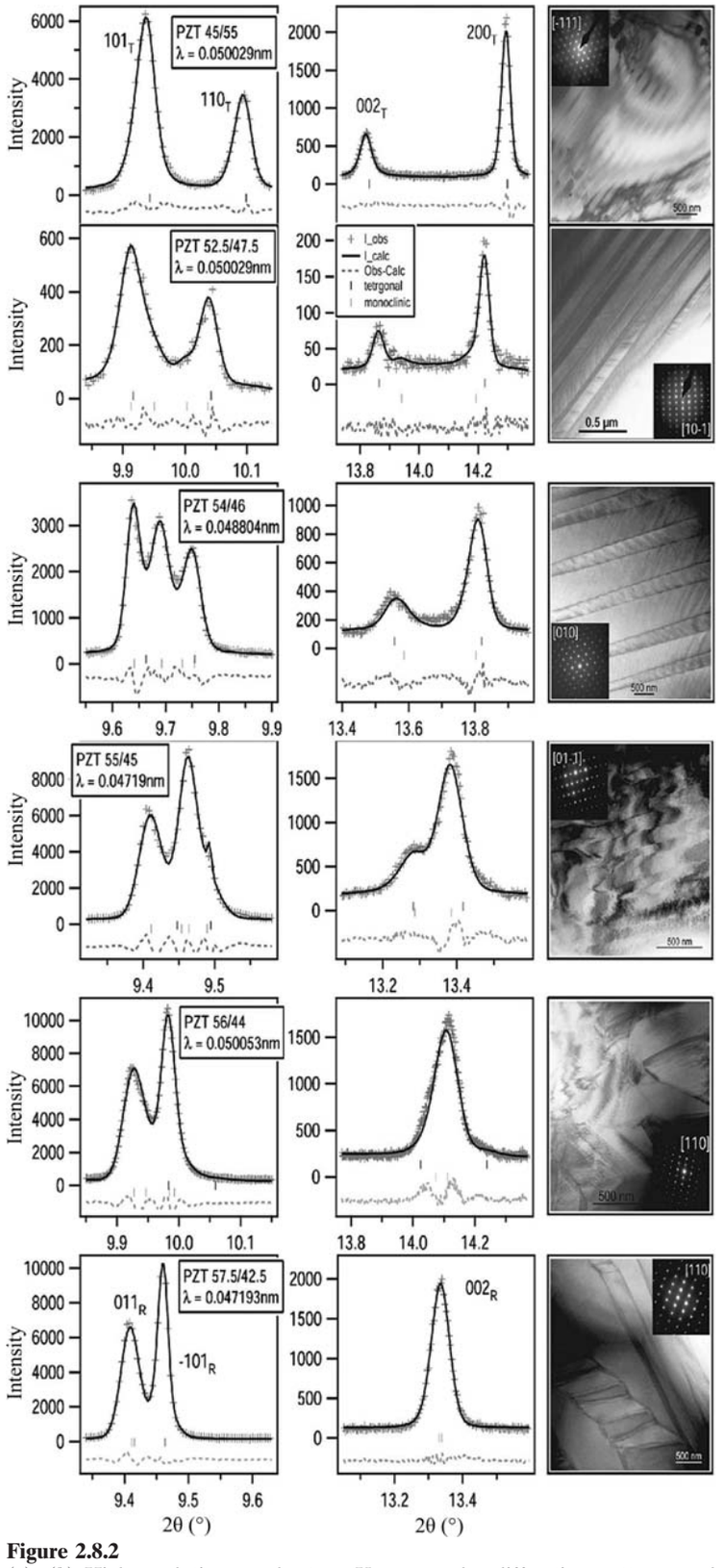

Figure 2.8.2
(*a*), (*b*) High-resolution synchrotron X-ray powder diffraction patterns and TEM imaging of PZT with a varying Zr/Ti ratio. An increase in broadening is seen in changes in shape and width of the 002_T reflection between the samples PZT 45/55, 52.5/47.5 and 54/46. The asymmetry and width of the tetragonal 101_T reflection not only change, but also evolve into a new peak between 101_T and 110_T in sample PZT 54/46, which gains in intensity towards PZT 57.5/42.5. This rise is accompanied by a decrease in intensity of the visible 110_T reflection, which then seems to be absent or overlapped in sample PZT 56/44. The domain structure changes from a lamellar tetragonal configuration *via* nanodomains to a rhombohedral herringbone structure. Reproduced with permission from Schönau, Schmitt *et al.* (2007). Copyright (2007) by the American Physical Society.

The different poling mechanisms can be studied in transmission geometry, which allows variation of the angle between the electric field vector **E** and the direction of the incident X-ray beam **k** from 0° to about 45° (Fig. 2.8.4) (Hinterstein *et al.*, 2011). Two sputtered electrodes (Ag, Pt) were used for polarization.

An extensive study under an electric field has been carried out on the commercially available sintered PZT material named PIC, in which Ti is partially replaced by Ni and Sb $[Pb_{0.99}Zr_{0.45}Ti_{0.47}(Ni_{0.33}Sb_{0.67})_{0.08}O_3]$, in transmission geometry. The angle between the electric field perpendicular to the flat sample surface and the incident beam was varied between 0 and 45°. The effect of domain switching in tetragonal symmetry mainly affects the $\{h00\}_C$ reflections, whereas the piezoelectric effect predominantly influences the $\{hhh\}_C$ reflections. Thus, the reflection pair 111_C and 200_C are the only reflections analysed in most studies. Fig. 2.8.5 displays just these reflections, with 200_C split into 002_T and 200_T, where the subscript 'T' refers to the tetragonal distorted cell, which is *translationengleich* to the cubic one (*i.e.* they have the same group of translations). The shift to higher angles of 111_C under an applied field indicates a decrease in volume. This is explained by the large angle between the electric field vector and the vector of spontaneous polarization for the unit cells contributing to 111_C. This induced compression remains in the remanent state.

While analysis of single reflections or orientations can yield valuable information on textured functional materials, a more sophisticated approach involves coupling the Eulerian angles to the diffraction patterns and modelling all observable mechanisms within a single refinement. By applying this method to a technically applied actuator material, Hinterstein, Hoelzel *et al.* (2015) could quantify all strain mechanisms and calculate the macroscopic response to an applied electric field with a structure model at the atomic scale.

The function of piezoceramics is related to periodic cycling of the polarization, accompanied by periodic changes of macroscopic strain. Fatigue in piezoceramic materials means that this strain is reduced as a result of the cycling; this has been studied with respect to the underlying structural changes (Hinterstein *et al.*, 2011, 2014).

Whereas strain is related to texturing, no preferred orientation is observed in fatigued samples. The orientation of nanodomains is demonstrated in different patterns: in Fig. 2.8.6 the two reflections are shown for the remanent state (0 kV mm^{-1}) at different diffraction angles and in Fig. 2.8.7 for values of the external field ranging from 0 to 2 kV mm^{-1}.

The diffuse scattering between the split 200_C reflections in the fatigued sample is reduced and the texturing increases after static poling for a few seconds. Thus, the fatigued samples show a more tetragonal appearance after cycling. The energy of the electric field induces a transition of well oriented nanodomains with preferred orientation along the field vector, leading to texturing for $\omega = 0°$. At a certain point the system will no longer respond to the electric field because of crack formation and a decrease in the volume of switchable nanodomains. From that point, the diffraction pattern recorded under a field is no different to the diffraction pattern recorded without a field.

Cyclic loading with high frequencies is required in real applications of ferroelectric ceramics. Exposure times

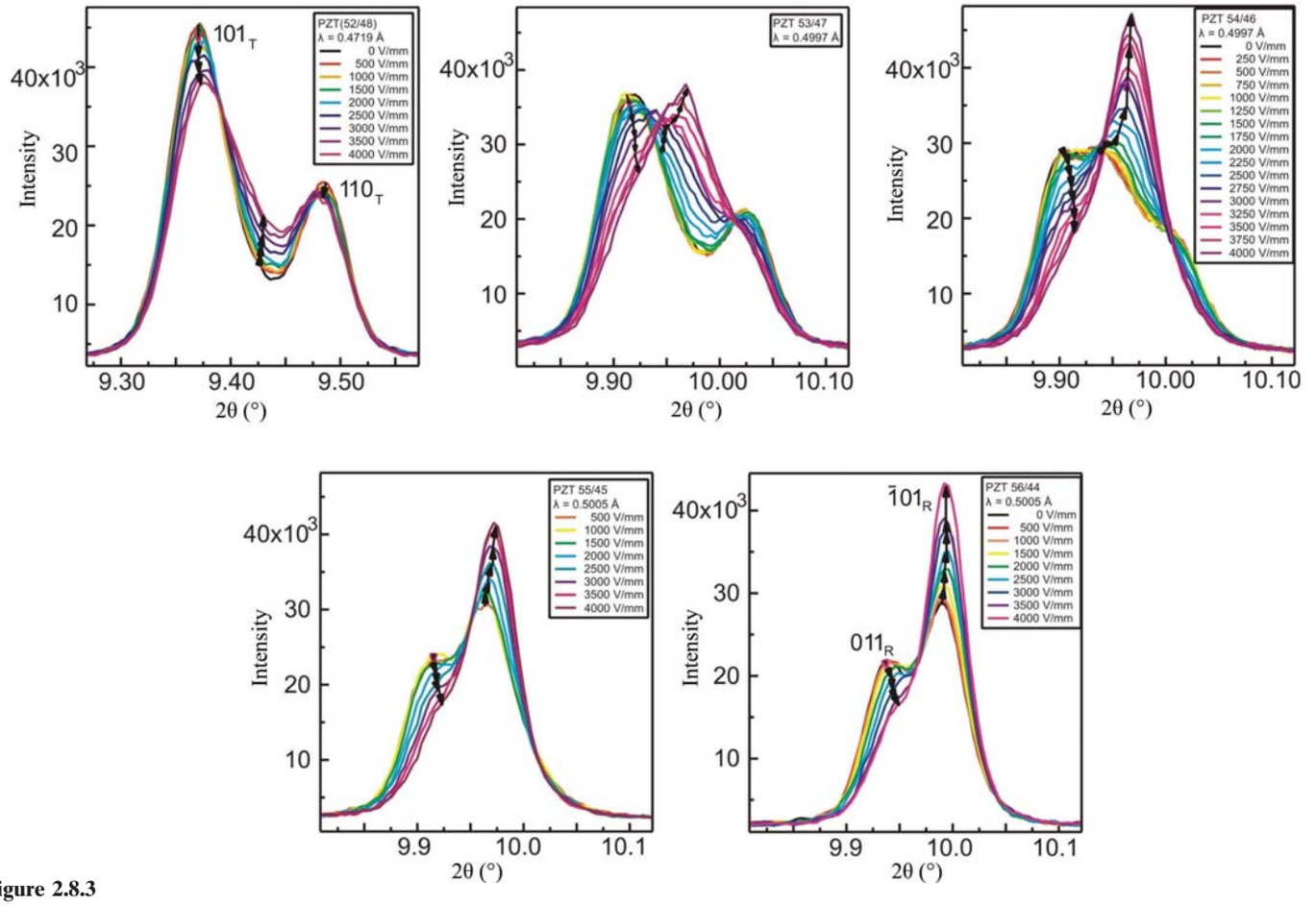

Figure 2.8.3
Diffraction patterns of the tetragonal 101_T /110_T reflection pairs of PZT 52/48, PZT 53/47, PZT 54/46, PZT 55/45 and PZT 56/44 recorded *in situ* under an electric field for the first poling cycle of up to 4 kV mm^{-1}. Reproduced with permission from Schönau, Knapp *et al.* (2007). Copyright (2007) by the American Physical Society.

in the range of seconds are necessary to ensure sufficient statistics for single diffraction experiments in the subsecond regime. Stroboscopic measurements can be used to achieve this.

Absolutely reversible processes are necessary for a successful stroboscopic analysis. The stability of the system is achieved by pre-cycling *circa* 10^5 times. Time resolutions in the range of several tens of milliseconds are possible with modern X-ray detectors. By repeating the excitation and summing the intensities, proper statistics can be achieved (Choe *et al.*, 2015; Hinterstein *et al.*, 2014).

The use of the stroboscopic data-collection technique and cyclic fields in neutron diffraction experiments enabled a direct measurement of non-180° domain wall motion during the application of subcoercive cyclic electric fields (Fig. 2.8.8) (Jones *et al.*, 2006, 2007; Jones, 2007; Daniels *et al.*, 2007). It was shown that the non-180° domain switching contributes 34% of the macroscopically measured strain during cycling with half of the coercive field.

The highest time resolutions are obtained in a pump–probe setup. Under the influence of an electric field of 2 kV mm^{-1}, the switching kinetics can be investigated directly. With a time

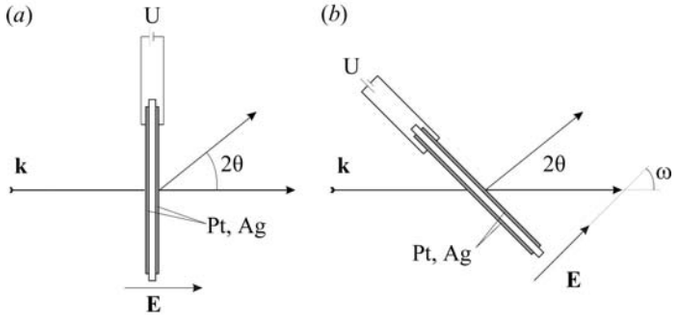

Figure 2.8.4
In situ transmission geometry developed by Schönau, Schmitt *et al.* (2007) with the electric field vector perpendicular to the flat-plate sample surface. The electric field results from an applied voltage U between two opposing sputtered electrodes (Ag, Pt) with a thickness of about 15 nm. (*a*) $\omega = 0°$ and (*b*) $\omega = 45°$.

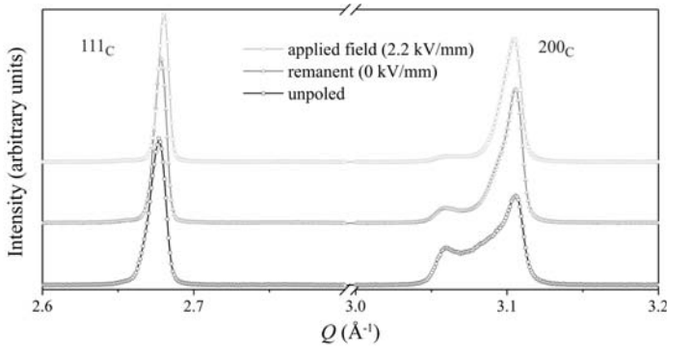

Figure 2.8.5
111_C and 200_C reflections of the unpoled, remanent and applied field state of PIC 151 at $\omega = 0°$. Owing to the piezoelectric effect, the 111_C reflection is shifted. The preferred orientation of the 200_C reflection indicates tetragonal 90° domain switching.

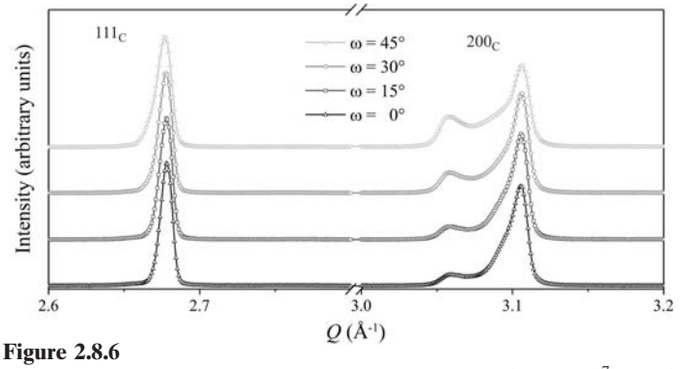

Figure 2.8.6
111_C and 200_C reflections of bipolar fatigued PIC 151 (50 Hz, 10^7 cycles) in the remanent state (0 kV mm^{-1} at $\omega = 0°$, 15°, 30° and 45°).

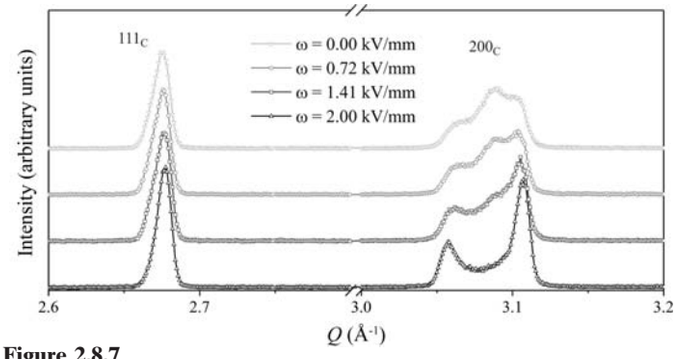

Figure 2.8.7
111_C and 200_C reflections of bipolar fatigued PIC 151 (50 Hz, 10^7 cycles) at $\omega = 45°$ with 0.0, 0.72, 1.41 and 2.0 kV mm^{-1}.

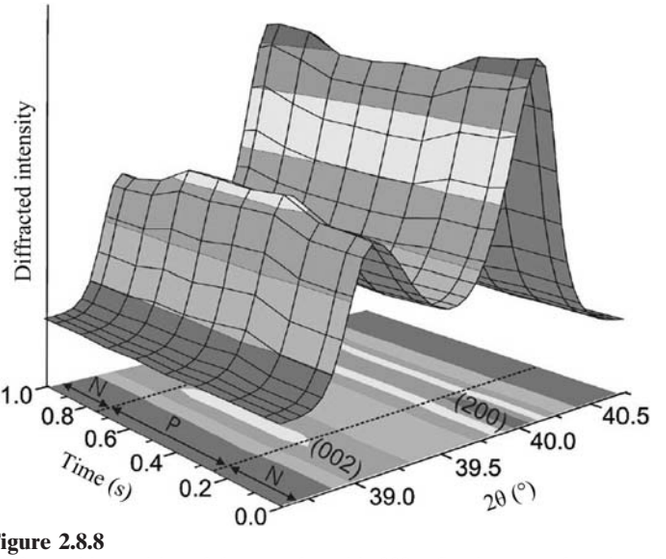

Figure 2.8.8
Diffracted intensities of the pseudo-cubic 002 reflections as a function of 2θ and time during application of a square, bipolar electric field waveform of frequency 1 Hz and amplitude of plus or minus half the coercive field. The timescale is described using eight steps. The positive (P) state of the electric field is applied between 0.25 and 0.75 s, which is bounded on either side by the negative (N) field state. The diffraction vectors 002 and 200 are parallel to the applied electric field. Reproduced with permission from Jones *et al.* (2006). Copyright (2006) AIP Publishing.

resolution of 1 ms only one intermediate step is observed (Fig. 2.8.9*a*). With a time resolution of 250 μs a significant number of intermediate steps can be studied (Fig. 2.8.9*b*). The commercially available soft-doped PZT material EC-65 has also been observed under the application of an electric field and mechanical stress. Lattice strains were measured under cyclic electric fields at times as short as 30 μs (Pramanick *et al.*, 2010).

The use of lead-containing materials may in the future be banned because of environmental concerns, hence considerable efforts are being made to find materials with properties similar to PZT. Only a few elements (Ba, Bi, Na, K, Nb, Ti) seem to be suitable. Nevertheless, a combination of the relevant oxides of these leads to a large variety of potential materials. $(Bi_{0.5}Na_{0.5})$-TiO_3–$BaTiO_3$ (BNT–BT) (Hinterstein, Schmitt *et al.*, 2015), $(Bi_{0.5}Na_{0.5})TiO_3$–$(Bi_{0.5}K_{0.5})TiO_3$ (BNT–BKT) (Levin *et al.*, 2013), BNT–BT–$K_{0.5}Na_{0.5}NbO_3$ (BNT–BT–KNN) (Schmitt *et al.*, 2010), BNT–BKT–KNN (Anton *et al.*, 2012) and BNT–KNN (Liu *et al.*, 2017) are the focus of most attention. The materials in the $(1 - x - y)$BNT–xBT–yKNN system exhibit remarkable piezoelectric properties over a narrow composition range $0.05 \leq x \leq 0.07$ and $0.01 \leq y \leq 0.03$ (Zhang *et al.*, 2007). Daniels *et al.* (2010) proposed a combinatorial approach to studying a range of compositions in a single sample, where different stoichiometries created a compositional gradient in the sample. A limited number of bulk homogeneous samples were prepared for comparison. Microfocus X-ray beams from a synchrotron allowed investigation of the gradient material under a field.

Fig. 2.8.10 displays the diffraction patterns under an external electric field up to 5.5 kV mm^{-1}. Data analysis was performed by fitting the data of the pseudo-cubic 002 reflection to distorted pseudo-cubic and tetragonal symmetry for each composition and electric field. Whereas in the 0.86BNT–0.14KNN composition only a distorted pseudo-cubic behaviour is observed

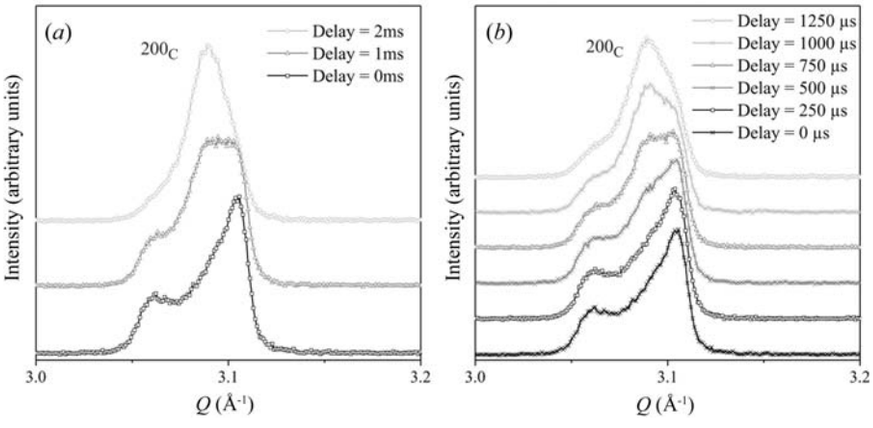

Figure 2.8.9
Pump–probe measurements of the 200_C reflection at $\omega = 45°$. Cycling switching between the remanent and the applied field state at 2 kV mm^{-1} with 50 Hz and a time resolution of (*a*) 1 ms and (*b*) 250 μs. Only a time resolution of 250 μs results in sufficient intermediate steps between the remanent and the poled state to study the processes during poling.

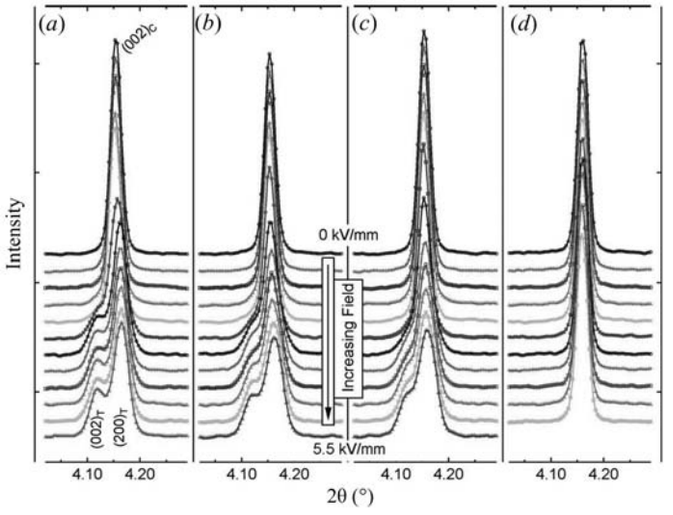

Figure 2.8.10
The pseudo-cubic 002 reflection of (*a*) 0.93BNT–0.07BT end member, (*b*) 0.938BNT–0.053BT–0.009KNN, (*c*) 0.932BNT–0.045BT–0.023KNN and (*d*) 0.86BNT–0.14KNN end member as a function of electric field from the initial zero-field state (top) to an applied field of 5.5 kV mm^{-1} (bottom). The sample orientation is such that the scattering vector is parallel to the electric field. Reproduced with permission from Daniels *et al.* (2010). Copyright (2010) Elsevier.

above a threshold of 0.5 kV mm^{-1}, a very pronounced distortion is observed for 0.93BNT–0.07BT, which eventually above 2 kV mm^{-1} develops into a tetragonal structure. In addition to the combination of various compositions, the authors simultaneously measured the X-ray fluorescence spectra, thus confirming the actual composition.

Fig. 2.8.11 depicts a Rietveld refinement of a lead-free ferroelectric material with the composition $0.92Ba_{0.5}Na_{0.5}TiO_3$–$0.06BaTiO_3$–$0.02K_{0.5}Na_{0.5}NbO_3$. New superstructure reflections (Fig. 2.8.11*b*, arrows) and a lattice distortion (Fig. 2.8.11*b*, circled) were observed due to a transition from space group *P*4*bm* to *R*3*c* (Hinterstein *et al.*, 2010).

In an overview, Jones summarized the use of diffraction techniques. Along with the importance of microdiffraction, diffuse scattering and texture effects, the importance of time-resolved studies including stroboscopy was acknowledged (Jones, 2007).

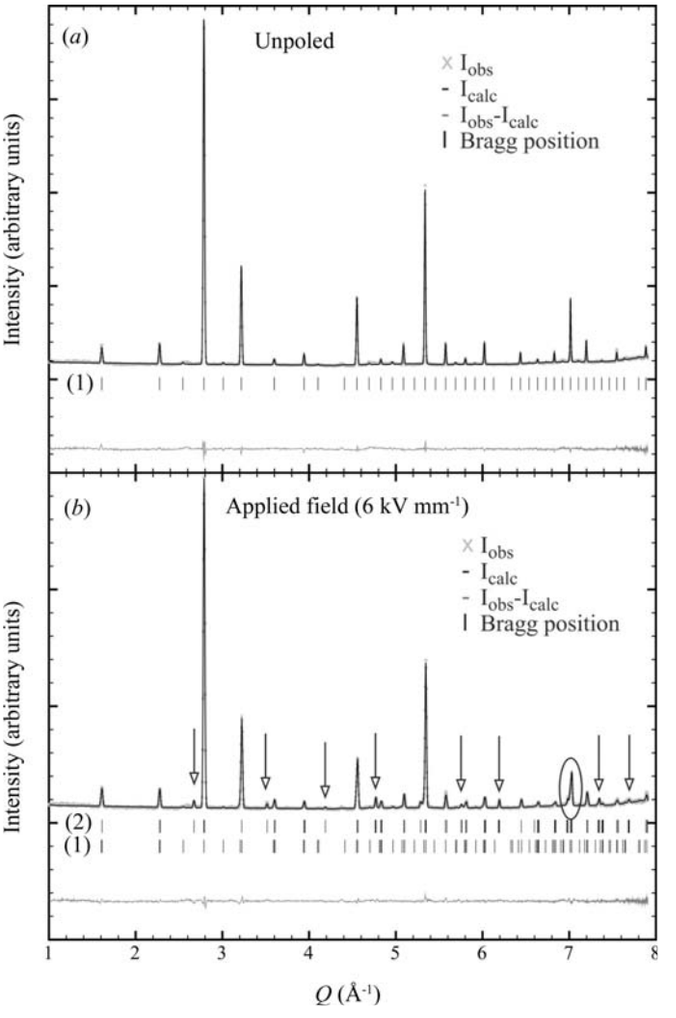

Figure 2.8.11
Rietveld refinement based on different patterns of $0.92Bi_{0.5}Na_{0.5}TiO_3$–$0.06BaTiO_3$–$0.02K_{0.5}NbO_3$ (*a*) in the unpoled and (*b*) in the applied field state at 6 kV mm^{-1}. Experimental data are shown by grey crosses, black lines denote calculated profiles, and the lower plot shows their difference. Calculated positions of Bragg reflections are shown by vertical tick marks, where the different rows correspond to the initial tetragonal phase with space group *P*4*bm* (1) and the field-induced rhombohedral phase with space group *R*3*c* (2). Arrows mark superlattice reflections of type $\frac{1}{2}\{ooe\}$ and the circle highlights the rhombohedral split 331_C reflection.

2.8.3.2. *In situ studies of electrode materials and in operando investigations of Li-ion batteries*

Rechargeable energy sources in mobile electronics are mainly based on lithium-ion batteries. Their application relies on the mobility of the small Li ions, which move from the cathode through an electrolyte to the anode during charge and back during discharge. Intensive research is underway to improve the performance of such energy-storage technology. High gravimetric and volumetric energy and power densities are required. Other additional challenges are safety, lifetime, the temperature range of stable operation and production costs per unit energy at the battery level. Knowledge of the correlation between the electrochemical functionality and the structure of the electrode materials during Li exchange is essential in order to interpret the underlying mechanisms and degradation processes and to find a promising approach to better materials. The high reactivity of the cell components and the very strong interactions between materials inside an electrochemical cell require studies on complete operational devices by non-invasive *in operando* methods. So-called electrochemical 'half cells' are often studied to follow structural changes in electrode materials. These are complete operational cells, but the electrode is cycled against an Li-metal counter electrode. Such half-cell studies are sometimes described as *in situ* studies. Limitations might occur with respect to fatigue studies and at very high charge and discharge rates, when the performance is determined by the Li-metal electrode. The classification of *in situ* and *in operando* methods is not unambiguous in structural studies on battery materials. Sometimes the term *quasi in situ* is used for studies where specific states of the materials are prepared electrochemically and handled in an Ar atmosphere with complete protection against humidity and air, but actually investigated *ex situ* (Oswald *et al.*, 2009).

Some early *in situ* setups have been described for neutron diffraction (Bergstöm, Andersson *et al.*, 1998) and transmission X-ray diffraction (Bergström, Gustafsson & Thomas, 1998), and also at elevated temperatures (Eriksson *et al.*, 2001). Today, for example, good-quality full diffraction patterns can be obtained

with exposure times well below 100 ms using synchrotron radiation (Herklotz *et al.*, 2013). Capillary-based micro-battery cells allow for *in situ* X-ray powder diffraction studies on one single electrode (Johnsen & Norby, 2013). Even spatially resolved neutron diffraction studies are possible on commercial cylindrical Li-ion batteries (Senyshyn *et al.*, 2015).

The mechanism of Li extraction and insertion differs for different types of electrodes. In intercalation-type electrodes the topology of the host structure remains mainly unchanged, and suitable sites in the structure are either occupied by Li or are vacant in the delithiated state. This use of intercalation chemistry for electrochemical energy storage was established for a battery based on Li metal as the negative electrode and TiS_2 as the positive electrode (Whittingham, 1976). In commercial cells today the negative electrode is also based on intercalation and consists of layered graphite, which hosts Li during the charge cycle up to the composition LiC_6. Another working mechanism for negative electrodes is electrochemical alloying with Li. The most promising examples involve Si, Al and Sn. These electrode concepts suffer from extreme volume changes: 100% for Al $\rightarrow$ LiAl or even 300% for Si $\rightarrow$ $Li_{21}Si_5$. In combination with the brittleness of these materials, the particles break down and become amorphous during successive charging and discharging, accompanied by contact losses and resulting pronounced fade in capacity. Two other mechanisms have also received considerable attention as they allow higher specific capacities. In a replacement reaction, one transition metal is replaced by Li while the topology of the structure is mainly preserved. During a conversion or displacement reaction the initial structures of transition-metal compounds, for example nanometre-sized oxides (Poizot *et al.*, 2000) or other binary compounds (Cabana *et al.*, 2010), are believed to be destroyed completely by either amorphization or phase transitions. The transition-metal ions are reduced to metallic nanoparticles, which are embedded in a complex network of Li_2O and reaction products from the electrolyte. In spite of the loss of long-range order, an important short-range structure remains. This has been shown in detail for ternary Cu–Fe oxides (Adam *et al.*, 2013). The reduction of Cu^{2+} from CuO takes place through the formation of a Cu_2O/Li_2O composite, in which Cu_2O reacts further to form Cu metal and Li_2O. Spinel-type $CuFe_2O_4$ and $CuFeO_2$ react to form α-$LiFeO_2$ with the extrusion of metallic Cu and Fe nanoparticles. At even lower potentials against Li^+/Li between 0.8 and 1.0 V, α-$LiFeO_2$ is further reduced into metallic Fe nanoparticles and Li_2O. While most of these displacement reactions suffer from very poor reversibility, good cycling stability was shown for $Cu_{2.33}V_4O_{11}$ (Morcrette *et al.*, 2003). During cell discharge Li penetrates into the well crystallized copper vanadate, forming a solid solution up to an Li content of $x = 0.6$, when Bragg peaks of metallic copper were observed. The end result was a composite electrode of an amorphous Li–V–O matrix with dispersed metallic copper. The essential point is the reversibility, with the disappearance of the metallic copper and the recrystallization of the initial $Cu_{2.33}V_4O_{11}$.

Two more examples belong to the class of intercalation materials: graphite as used for the negative electrode, and $LiNiO_2$ as a candidate for the positive electrode. 'Positive' and 'negative' electrodes are the preferred terms for secondary batteries instead of 'cathode' and 'anode', because anode and cathode reactions match only for discharge (interchange between the two electrodes occurs for the charge process). A comprehensive summary of structure reports on lithiated graphite can be found in Johnsen & Norby (2013). From the voltage plateau in cyclovoltammograms four distinct lithiated graphite phases have been postulated. However, only for two of them have complete structure models been reported and confirmed. The first is LiC_{12}, *P*6/*mmm* (space group No. 191), $a = 4.29$, $c = 7.03$ Å, with C on the 12*n* site with $x = 0.33$ and $z = 0.25$ and Li on the 1*a* site; the second is LiC_6, also *P*6/*mmm*, $a = 4.31$, $c = 3.70$ Å with C on the 6*k* site with $x = 0.33$ and Li again on the 1*a* site. According to the number of graphene layers that are needed for the smallest unit repeated by translational symmetry along the sixfold rotation axis, these structures are described as stage-II (LiC_{12}) and stage-I (LiC_6) compounds, like graphites intercalated with other alkaline elements. Note that in these phases the graphene layers are not shifted with respect to each other (*AA* sequence), in contrast to graphite (*AB* sequence). For a lower Li content, a much more complex structural behaviour was observed, including incommensurate Li distributions between the graphene layers, which were described as twisted bilayers (Senyshyn *et al.*, 2013). Higher-order reflections were observed for these phases and allowed indexing with a propagation vector (α, α, 0). Different structure models were discussed, but a complete description of the Li distribution is still lacking. Therefore, it is still an open question as to where the Li atoms in lithiated graphite are at low Li contents (below 1 Li per 12 C).

$LiNiO_2$ is considered to be a promising positive electrode material (Ohzuku *et al.*, 1993). However, it has some limitations, which are directly linked to the underlying structure. A high degree of cation disorder, *i.e.* Li on the Ni site and *vice versa*, hinders Li transport within the layers. Furthermore, Li and Ni exchange takes place rather easily, in contrast to $LiCoO_2$, because of a more favourable transport process through a tetrahedral interstitial site for Ni than for Co. In the cases of Li excess, $Li_{1+\delta}NiO_2$, or Ni excess, $(Li_{1-\delta}Ni_\delta)NiO_2$, some Ni^{2+} ions exist, which have a very similar ionic radius to that of Li^+. Therefore, it is nearly impossible to prepare stoichiometric $LiNiO_2$ with perfect separation of Li and Ni onto distinct layers. The best samples with respect to cation order are obtained from $NaNiO_2$ by successive Na $\rightarrow$ Li ion-exchange reactions. These drawbacks have prevented the commercial application of $LiNiO_2$, and more complex materials like $Li(Ni,Co,Al)O_2$ (NCA) and $Li(Ni,Co,Mn)O_2$ (NCM) are increasingly replacing $LiCoO_2$. Fig. 2.8.12 shows the structural changes in $LiNiO_2$ during the first charge and discharge. The detailed experimental conditions are the same as those described by Nikolowski *et al.* (2005) for $Li(Ni_{0.8}Co_{0.2})O_2$. One of the most characteristic features of the structural response to Li extraction and insertion is the pronounced change in the lattice parameters, shown by the changes in the *c*/*a* ratio for the rhombohedral structure. During Li extraction the *c* parameter increases, because there are fewer Li ions between (repulsive) O-atom layers. However, at lower Li contents, some of the O ions become oxidized, and the repulsion between the O-atom layers is weaker, resulting in shorter *c*-axis parameters. As a general rule, all layered oxides $LiMO_2$, with *M* = Mn, Co and/or Ni, become intrinsically unstable in the highly delithiated states beyond the maximum in the *c*/*a* ratio. Note that the as-prepared material has a very high degree of cation disorder (9.3% Ni on the Li site) and very poor capacity retention in the second cycle. The initial phase (*A*) gradually disappears and apparently transforms into a second phase (*B*) with a much lower degree of cation disorder (less than 3%). Note that this phase sequence does not necessarily reflect equilibrium conditions, but depends strongly on the chemical composition (Li or Ni excess), microstructure (size and strain) and the experimental conditions (charge rate, temperature, electrode formulation and more).

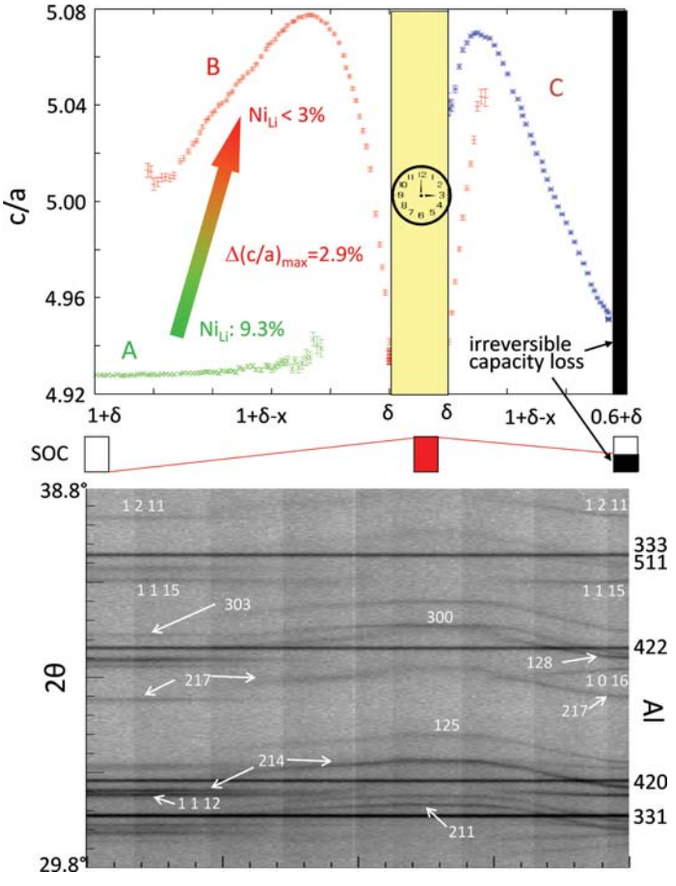

Figure 2.8.12
$Li_{1+\delta}NiO_2$ during charge and discharge. From about 210 complete diffraction patterns [a small section is shown below (λ = 0.499366 Å)], the structural response to Li extraction and insertion was monitored. In addition to changes in the unit-cell metric, the distribution of Li and Ni onto layers becomes more ordered during the first highly charged state. A pronounced capacity loss is observed during discharge after a holding time of 3 h in this overcharged state. A, B and C are three successively appearing phases. SOC = state of charge.

Such *in situ* studies are very important for elucidating the working mechanism and degradation processes for intercalation electrodes (Senyshyn *et al.*, 2012). Nevertheless, complementary methods are also essential for providing all the necessary information, especially about the surface near-interface region between the electrode and electrolyte, which has to be studied with surface-sensitive and local methods.

2.8.3.3. *Diffraction under a magnetic field*

2.8.3.3.1. *General remarks*

The majority of synchrotron and neutron experiments are currently limited to superconducting magnets with fields of 5–16 T. When higher fields are required there are essentially two possible solutions: pulsed resistive or steady-field resistive (or hybrid: resistive inner coil, superconducting outer coil) magnets. Pulsed fields are often used when signals are strong and the signal-to-noise ratio is good, whereas steady fields are primarily used for techniques with relatively long counting times and many data points. The relatively short pulse duration (from microseconds to milliseconds) along with the rather large sample volume required severely limit the use of pulsed magnetic fields in powder diffraction applications as well as more exotic methods of achieving high magnetic fields, *e.g.* magnetic flux compression or single-turn coils (Schneider-Muntau *et al.*, 2006). Furthermore,

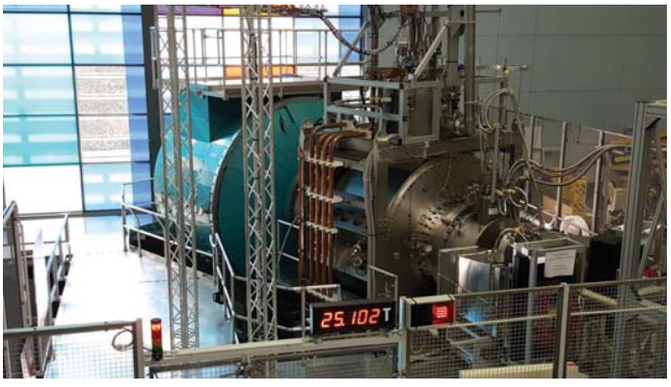

Figure 2.8.13
The High Magnetic Field Facility for Neutron Scattering at the Helmholtz-Zentrum Berlin has two main components: the High Field Magnet (HFM) and the Extreme Environment Diffractometer (EXED). Courtesy of Dr O. Prokhnenko.

because of the large stresses, the lifetime of a resistive/pulsed magnet is finite: pulsed magnets have typical lifetimes of 500 shots at 95% of the design field, and their lifetimes are virtually independent of pulse duration.

At present, the maximum field for technical superconductors is 23 T and modern developments in superconductor design along with robust magnet manufacturing techniques have made possible high-flux-density magnets for neutron scattering studies up to 16 T. For resistive magnets, there are in principle no limitations to the generation of the highest continuous fields apart from economics, as approximately 1 MW of electric power is consumed per 1 T field strength. Therefore, in order to reduce the running costs (*i.e.* the required power per unit magnetic field), hybrid magnets are becoming increasingly popular. In this context we mention the joint developments between the National High Magnetic Field Laboratory (Tallahassee, FL, USA), the Spallation Neutron Source (Oak Ridge, TN, USA) and Helmholtz-Zentrum Berlin (Germany) in the development of high-steady-field (25 T with a 4 MW resistive insert, 30 T with an 8 MW resistive insert) hybrid magnets for neutron scattering (Bird *et al.*, 2009). A high-field magnet has been installed and is in routine user operation (Fig. 2.8.13) at the Extreme Environment Diffractometer (HFM-EXED) of Helmholtz-Zentrum Berlin (Prokhnenko *et al.*, 2015).

On the other hand, it is quite simple to produce magnetic flux density uniformity or homogeneity over the required sample volume down to the p.p.m. level with a solenoid magnet. However, the majority take the form of split-pair solenoids. With this setup, the access to the sample environment (along the magnetic axis) can be orthogonal to the beam-access plane. The split-coil setup is the most popular in neutron scattering, but the geometry constraints imposed by the neutron aperture make the creation of very uniform flux density much more difficult. In general, for a typical neutron-scattering sample volume of 1 cm^3, the magnetic field homogeneity is normally limited to the range 0.1 to 5%. As the available current density for a given conductor decreases with increasing flux density, the flux density seen by the superconductor inside the magnet windings is greater than the 'nominal' central value. This is particularly the case for split-pair magnets, where the ratio of the two can be large, *e.g.* for a central value of 9 T, a ratio of 1.6 gives a maximum flux density of 14.3 T (Brown, 2010).

As already pointed out, diffraction studies under a magnetic field are almost always performed with neutrons. However,

Mitsui *et al.* (2009) have developed a device that includes a cryo-cooled split-pair NbTi superconducting magnet and a sample furnace, for high fields and temperatures above room temperature, respectively, which can be installed on a laboratory X-ray diffractometer. The magnetic field generated goes up to 5 T at the centre of a 50 mm vertical and 10 mm horizontal bore, with a field homogeneity of 0.1%. The first results of studies on the martensitic phase transition in the shape memory system $Ni_{40}Co_{10}Mn_{34}Al_{16}$ in a field of 5 T and at temperatures up to 473 K have been reported for powders (Mitsui *et al.*, 2009).

Synchrotron radiation can be used to study specific properties such as orbital contributions and their separation from the spin values. Diffraction studies with unpolarized neutrons are common at a constant field to elucidate simple magnetic structures: no confident conclusion about the spin direction can be obtained if the configurational symmetry is cubic, and in the case of uniaxial symmetry (either tetragonal, hexagonal or rhombohedral) only the angle with the unique axis of the magnetic structure can be defined (Shirane, 1959). The sensitivity of non-polarized neutron powder diffraction (the magnetic detection limit) is by a few orders of magnitude less than that of superconducting quantum interference device (SQUID) magnetometry, muon spin rotation or magnetic dichroism spectroscopy. In an antiferromagnetically ordered system the determination of magnetic moments below 0.1 μ_B per magnetic atom presents severe challenges, which become even more pronounced for the localization of weak ferromagnetic components. Less frequent are *in situ* investigations to determine magnetic phase diagrams. The use of powder samples at high magnetic fields is often limited by the redistribution of grains and texture effects.

Experiments with polarized neutrons are normally performed with single crystals. Out of the variety of compounds that have been studied, we have chosen materials with particular properties and report on *in situ* studies of them under magnetic fields.

2.8.3.3.2. *Frustrated magnetic systems*

Multiferroic systems (or more precisely magnetoelectric materials) have gained considerable attention because of their potential applications in devices. In fact, the efficient control of magnetism by an electric field allows magnetic information to be written electrically (with low energy consumption) and read magnetically. A real application, however, requires both phenomena to occur at room temperature. There are very few compounds that fulfil this requirement; examples include $BiFeO_3$ and β-$NaFeO_2$.

Magnetoelectric properties have been observed in many compounds with different structures and chemical compositions. However, they all have a geometrical magnetic frustration in common, which induces competition among multiple magnetic ground states. Furthermore, a magnetic phase transition is thought to be an essential ingredient for realizing a non-linear colossal response in the electric properties. In the colossal effect, the two properties not only coexist but couple strongly in their order parameter. Most novel multiferroic materials exhibit a cycloidal component to the magnetic structure; this has been considered as a guiding principle for tailoring new materials based on the non-collinearity of the spins. Many cycloidal compounds exhibit a small ferromagnetic component in their antiferromagnetic order, giving rise to the Dzyaloshinskii–Moriya interaction. We shall concentrate here on two systems linked by frustration in the magnetic ordering, namely orthovanadates and the manganites of the rare earths.

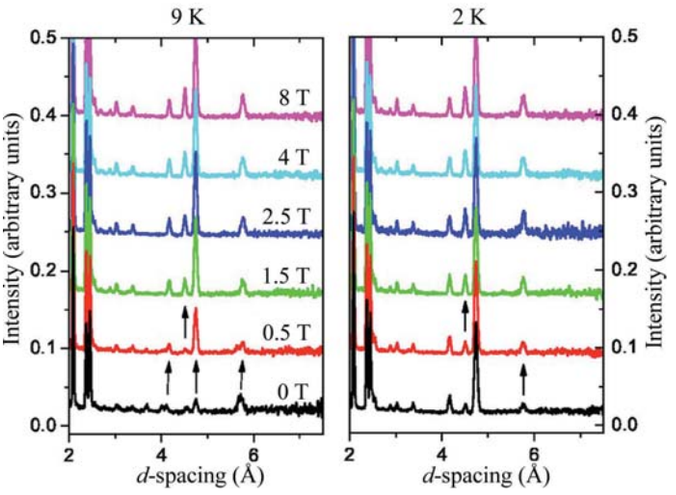

Figure 2.8.14
Neutron powder diffraction data for $Co_3V_2O_8$ at 9 K (left) and 2 K (right) under magnetic fields of 0, 0.5, 1.5, 2.5, 4.0 and 8.0 T. Data from a bank of detectors situated at the scattering angle 35° are shown. The arrows indicate the changes between the data at different fields. Individual curves are offset arbitrarily for display purposes. Reprinted with permission from Wilson *et al.* (2007). Copyright (2007) by the American Physical Society.

2.8.3.3.2.1. *Kagomé staircase systems*

Among the orthovanadates of 3*d* metals, $Co_3V_2O_8$ and $Ni_3V_2O_8$ have been identified as kagomé staircase magnetic structures, which exhibit a considerable number of phase transitions at low temperature. Their crystal structure was determined by Fuess *et al.* (1970) as orthorhombic (space group *Cmca*). Ferromagnetic order was found for the cobalt compound and an indication of antiferromagnetism for the nickel compound at 4.2 K. The crystal structure is characterized by edge-sharing CoO_6 octahedra forming buckled layers of corner-sharing triangles, called kagomé staircases, separated by VO_4 tetrahedra. The magnetic ions (Co or Ni) are situated at the corners of triangles, thus leading to spin frustration. Therefore, if a small amount of energy is supplied by an external magnetic field, a whole sequence of magnetic phase transitions can be introduced. The previously determined ferromagnetic order as the ground state for $Co_3V_2O_8$ was confirmed by Wilson *et al.* (2007). They also reported field-dependent neutron powder diffraction studies under a field of 8 T at 2 and 9 K (Fig. 2.8.14). At 9 K the system has an incommensurate magnetic structure. At a field as low as 0.5 T, new magnetic peaks indexed in a commensurate structure occur, accompanied by a shift in the position of others. The incommensurate ordering disappears completely at a higher field and a purely ferromagnetic behaviour is observed, similar to the low-temperature ground state at zero field. At 2 K and 8 T no additional magnetic reflections are observed but changes in the intensity of several existing ones are seen. The refinement of the magnetic structure based on these data indicated a change of the spin direction in the ferromagnetic arrangement as compared with the zero-field low-temperature structure. Furthermore, the magnetic moments on the two different Co sites in the structure are aligned under the field and reach the same value of 3.15 μ_B on both sites, which is similar to the spin-only moment of cobalt.

The reorientation of spins and the complete magnetic field *versus* temperature (*H*–*T*) phase diagram of the multiferroic $Ni_3V_2O_8$ has been reported (Kenzelmann *et al.*, 2006). The inversion symmetry of space group *Cmca* is broken at low temperature and a commensurate phase is observed. Thus, over a

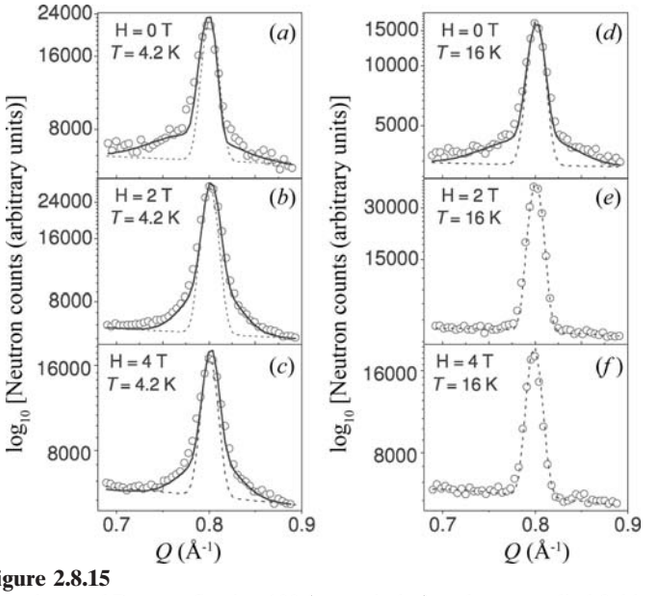

Figure 2.8.15
The observed Bragg reflection 100 (open circles) under an applied field of (*a*) 0 T, (*b*) 2 T and (*c*) 4 T at 4.2 K and (*d*) 0 T, (*e*) 2 T and (*f*) 4 T at 16 K (taken from Yusuf *et al.*, 2013). Copyright IOP Publishing. Reproduced with permission. All rights reserved.

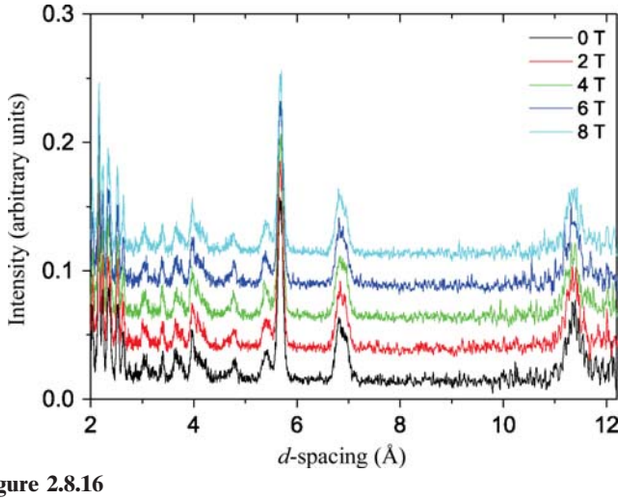

Figure 2.8.16
Time-of-flight diffraction patterns of YMn_2O_5 at 1.6 K under magnetic fields between 0 and 8 T (taken from Radaelli & Chapon, 2008). Copyright IOP Publishing. Reproduced with permission. All rights reserved.

narrow temperature range a macroscopic polar vector leads to a multiferroic behaviour. As this study was based on single-crystal neutron measurements, no further details are given here. Frustrated triangular-lattice Ising antiferromagnets have degenerate magnetic ground states, which give rise to very complex magnetic structures. As there are only small differences in the competing exchange interaction in such frustrated triangular-lattice compounds, a sequence of phase transitions is introduced by changes in temperature or magnetic field. The compound $Ca_3Co_2O_6$ is another example of a frustrated system. Field-dependent powder diffraction patterns were reported for the doped system $Ca_3Co_{1.8}Fe_{0.2}O_6$ by Yusuf *et al.* (2013). They distinguished the short-range magnetic order (SRO), reflected in the half-width of the Bragg reflections (Fig. 2.8.15), from the long-range order as given by the Bragg positions. They stated that even under magnetic fields up to 4 T the broadening of Bragg reflections indicates the persistence of SRO. In a field of 2 T, the observed change in the structure from incommensurate to commensurate indicates a reduction of spin frustration. In fields of 4 T, a ferrimagnetic system is introduced, followed by a ferromagnetic one above 5 T.

2.8.3.3.2.2. Manganite systems

Like the vanadates, in the class of rare-earth manganites of the type RMn_2O_5 successive magnetic phase transitions between commensurate (CO) and incommensurate phases (ICP) can occur. Intensive investigations have been undertaken to understand the relationship between their magnetic and dielectric properties. The spontaneous electric polarization is induced by a magnetic transition. Thus the primary order parameter is magnetic rather than structural. Among the rare-earth compounds, those containing Nd or an element lighter than Nd do not exhibit ferroelectricity. In all these materials a broken magnetic symmetry at lower temperatures leads to a polar symmetry group. In addition, a cycloidal component indicates a common underlying mechanism. The Mn^{3+} and Mn^{4+} ions are fully charge-ordered. Neutron diffraction studies of these phases have been performed by Radaelli & Chapon (2008), who also analysed the possible exchange pathways. In $TbMn_2O_5$ the *H*–*T* phase diagram of the commensurate–low-temperature–incommensurate (CO–LT–ICP) magnetic transitions shows an upward jump in the transition temperature from ∼25 K at zero field to 27 K at 9 T. The low-temperature ICP phase is stabilized under an external field for $TbMn_2O_5$ and the dielectric constant is enhanced. It was concluded that Tb and Mn order independently, implying the absence of coupling terms between them. Strong support for this suggestion was provided by an in-field neutron study on the analogue YMn_2O_5. Neither the positions nor the intensities of the magnetic Bragg reflections were affected by the magnetic field (Fig. 2.8.16). The magnetic low-temperature ICP phase in the Tb compound was stabilized under a magnetic field. This is in contrast to observations on $HoMn_2O_5$ by Kimura *et al.* (2007), using single crystals. In both cases, however, the neutron data correlate directly with the results obtained by dielectric measurements under a magnetic field. The difference in the behaviours is thus confirmed. The two studies also reveal different magnetic order at low temperatures. The same magnetic sequence at low temperatures as for Tb was observed in YMn_2O_5, which does not contain a magnetic rare-earth element. Under fields up to 8 T the positions and the intensities of the magnetic Bragg reflections remained unchanged, showing that the antiferromagnetic structure of the manganese sublattice is extremely stable. As in the vanadates, the main reason for the sequence of magnetic structures is frustration of the manganese spins. Without going too deeply into the details of the different exchange pathways and orbital occupancies, one factor behind this behaviour is the Jahn–Teller effect of the Mn^{3+} ion, which is also relevant in the multiferroic $TbMnO_3$ as part of the $RMnO_3$ family (Kimura *et al.*, 2003). Another feature often found in multiferroic systems is the small ferromagnetic component caused by small spin canting due to Dzyaloshinskii–Moriya interactions. This property strongly influences the low-temperature magnetism in RMn_2O_5 (Kimura *et al.*, 2009).

2.8.3.3.3. *Additional systems and scattering techniques*

Information about the anisotropy of the local magnetic susceptibility at different magnetic sites has been extracted from diffraction patterns for a $Tb_2Sn_2O_7$ powder measured using polarized neutrons under magnetic fields of 1 and 5 T (Gukasov

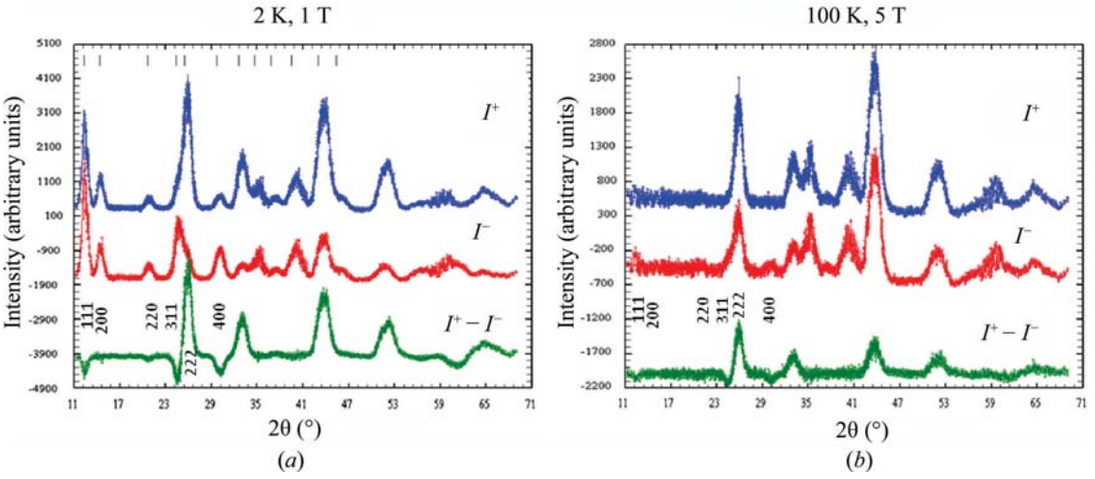

Figure 2.8.17
Polarized neutron diffraction patterns for $Tb_2Sn_2O_7$ at 2 K and 1 T (*a*) and 100 K and 5 T (*b*). I^+ and I^- are the intensities for spin-up and spin-down neutrons, respectively. Taken from Gukasov & Brown (2010). Copyright IOP Publishing. Reproduced with permission. All rights reserved.

& Brown, 2010). No magnetic contribution to the diffracted intensities was observed at 2 K in the absence of an external field. However, applying a field led to considerable changes in the diffraction pattern (Fig. 2.8.17). At 100 K and 5 T, the intensities of the reflections that are allowed for the cubic space group $Fd\bar{3}m$ increase considerably. Furthermore, they were found to depend strongly on the polarization of the incoming neutrons, as shown by the difference pattern in Fig. 2.8.17. At a field of 1 T, new reflections appear (Fig. 2.8.17*a*) that are forbidden for the occupied sites in $Fd\bar{3}m$ symmetry, such as 200, 222 and 240. The intensities of these new reflections do not change with the polarization of the neutrons, as demonstrated in the difference plot, hence they are purely magnetic. In conclusion, information on local anisotropic magnetic susceptibility at different sites can be obtained by using a combination of unpolarized and polarized neutron powder patterns. This demonstrates the usefulness of polarized neutron scattering, even for polycrystalline samples.

We now return to X-ray investigations of magnetic materials. A laboratory device for fields up to 5 T and temperatures above room temperature was mentioned in Section 2.8.3.3.1. The corresponding low-temperature apparatus (Koyama *et al.*, 2013) has produced results on magneto-caloric compounds of MnFeP-type materials. Substitution of P in $MnFeP_{1-x}Z_x$ with Z = As or Ge produces materials that exhibit a large magneto-caloric effect and thus allows control of the Curie temperature by chemical composition. Studies under magnetic fields are mandatory, as the refrigerants are working under a field. For two different compositions of the As compound the lattice parameters change drastically and the cell volume decreases with increasing magnetic field strength. In $MnFeP_{0.78}Ge_{0.22}$ a field-induced ferromagnetic phase was observed near the Curie temperature at 280 K. This phase is, however, not identical to the low-temperature ferromagnetic one (Koyama *et al.*, 2013).

2.8.3.3.4. *Concluding remarks*

Despite some shortcomings, powder diffraction studies as a function of magnetic fields are valuable for the qualitative and sometimes even quantitative interpretation of magnetic materials. Unpolarized neutrons are used in most experiments, but the additional information from polarized neutrons has also been exploited. X-rays do not interact directly with the magnetic moments, but structural changes as a consequence of magnetic phase transitions have been observed in several cases. *In situ* powder diffraction under magnetic fields reaching 4 T on an X-ray diffractometer with a rotating anode revealed details of lattice parameters and atomic positions in rare-earth alloys with a higher precision than that accessible by neutron diffraction (Pecharsky *et al.*, 2007). Furthermore, the two test-case compounds studied, Gd_5Ge_4 and $DyCo_2$, contain the rare-earth elements Gd and Dy with the highest absorption cross sections for neutrons in their natural isotope abundance. The data were used to refine the underlying structure models by Rietveld analysis. Advances in X-ray and neutron sources and optics delivered higher resolution and flux to the samples, which in combination with rapid computing made real-time experiments feasible.

2.8.4. Summary

We have shown here that *in situ* studies under electric and magnetic fields are in a well advanced state. Laboratory equipment can be used for diverse experiments where changes occur on a timescale that can be followed with an exposure time of minutes. Real progress is, however, achieved by using high-energy synchrotron radiation and by using neutrons, which can penetrate larger volumes. Thus *in operando* studies of real devices are feasible. In addition to such diffraction experiments, which provide average information on a macroscopic length scale, complementary experiments like electron microscopy are vital for revealing local structural information. Only the combination of several methods can give sufficient insight into structure–property relationships and the functionality of materials.

References

Adam, R., Wadewitz, D., Gruner, W., Klemm, V., Ehrenberg, H. & Rafaja, D. (2013). *Phase and microstructure development in the conversion type electrodes for Li-ion batteries based on the Cu-Fe-O system. J. Electrochem. Soc.* **160**, A1594–A1603.

Anastasopoulos, M., Bebb, R., Berry, K., Birch, J., Bryś, T., Buffet, J.-C., Clergeau, J.-F., Deen, P. P., Ehlers, G., van Esch, P., Everett, S. M., Guerard, B., Hall-Wilton, R., Herwig, K., Hultman, L., Höglund, C., Iruretagoiena, I., Issa, F., Jensen, J., Khaplanov, A., Kirstein, O., Higuera, I. L., Piscitelli, F., Robinson, L., Schmidt, S. & Stefanescu, I. (2017). *Multi-grid detector for neutron spectroscopy: results obtained on time-of-flight spectrometer CNCS. J. Instrum.* **12**, P04030.

Anton, E.-M., Schmitt, L. A., Hinterstein, M., Trodahl, J., Kowalski, B., Jo, W., Kleebe, H.-J., Rödel, J. & Jones, J. L. (2012). *Structure and temperature-dependent phase transitions of lead-free $Bi_{1/2}Na_{1/2}TiO_3$–$Bi_{1/2}K_{1/2}TiO_3$–$K_{0.5}Na_{0.5}NbO_3$ piezoceramics. J. Mater. Res.* **27**, 2466–2478.

Ballabriga, R., Campbell, M., Heijne, E. H. M., Llopart, X. & Tlustos, L. (2007). *The Medipix3 prototype, a pixel readout chip working in single photon counting mode with improved spectrometric performance. IEEE Trans. Nucl. Sci.* **54**, 1824–1829.

Bergamaschi, A., Cervellino, A., Dinapoli, R., Gozzo, F., Henrich, B., Johnson, I., Kraft, P., Mozzanica, A., Schmitt, B. & Shi, X. (2009). *Photon counting microstrip detector for time resolved powder diffraction experiments. Nucl. Instrum. Methods Phys. Res. A*, **604**, 136–139.

Bergström, Ö., Andersson, A. M., Edström, K. & Gustafsson, T. (1998). *A neutron diffraction cell for studying lithium-insertion processes in electrode materials. J. Appl. Cryst.* **31**, 823–825.

Bergström, O., Gustafsson, T. & Thomas, J. O. (1998). *An X-ray powder diffraction attachment for in situ studies of ion insertion processes in electrode materials. J. Appl. Cryst.* **31**, 103–105.

Bird, M. D., Hongyu Bai, Bole, S., Jingping Chen, Dixon, I. R., Ehmler, H., Gavrilin, A. V., Painter, T. A., Smeibidl, P., Toth, J., Weijers, H., Ting Xu & Zhai, Y. (2009). *The NHMFL hybrid magnet projects. IEEE Trans. Appl. Supercond.* **19**, 1612–1616.

Brown, F. J. (2010). *Aspects of superconducting magnet design for neutron scattering sample environments. J. Phys. Conf. Ser.* **251**, 012093.

Cabana, J., Monconduit, L., Larcher, D. & Palacín, M. (2010). *Beyond intercalation-based Li-ion batteries: the state of the art and challenges of electrode materials reacting through conversion reactions. Adv. Mater.* **22**, E170–E192.

Cartier, S., Bergamaschi, A., Dinapoli, R., Greiffenberg, D., Johnson, I., Jungmann, J. H., Mezza, D., Mozzanica, A., Schmitt, B., Shi, X., Stampanoni, M., Sun, J. & Tinti, G. (2014). *Micron resolution of MÖNCH and GOTTHARD, small pitch charge integrating detectors with single photon sensitivity. J. Instrum.* **9**, C05027.

Choe, H., Gorfman, S., Hinterstein, M., Ziolkowski, M., Knapp, M., Heidbrink, S., Vogt, M., Bednarcik, J., Berghäuser, A., Ehrenberg, H. & Pietsch, U. (2015). *Combining high time and angular resolutions: time-resolved X-ray powder diffraction using a multi-channel analyser detector. J. Appl. Cryst.* **48**, 970–974.

Daniels, J. E. & Drakopoulos, M. (2009). *High-energy X-ray diffraction using the Pixium 4700 flat-panel detector. J. Synchrotron Rad.* **16**, 463–468.

Daniels, J. E., Finlayson, T. R., Studer, A. J., Hoffman, M. & Jones, J. L. (2007). *Time-resolved diffraction measurements of electric-field-induced strain in tetragonal lead zirconate titanate. J. Appl. Phys.* **101**, 094104.

Daniels, J. E., Jo, W., Rödel, J., Honkimäki, V. & Jones, J. L. (2010). *Electric-field-induced phase-change behavior in* $(Bi_{0.5}Na_{0.5})TiO_3$–$BaTiO_3$–$(K_{0.5}Na_{0.5})NbO_3$*: a combinatorial investigation. Acta Mater.* **58**, 2103–2111.

Eckold, G., Schober, H. & Nagler, S. E. (2010). Editors. *Studying Kinetics with Neutrons. Springer Series in Solid State Sciences.* Berlin, Heidelberg: Springer.

Eriksson, T., Andersson, A. M., Bergström, Ö., Edström, K., Gustafsson, T. & Thomas, J. O. (2001). *A furnace for in situ X-ray diffraction studies of insertion processes in electrode materials at elevated temperatures. J. Appl. Cryst.* **34**, 654–657.

Fuess, H., Bertaut, E. F., Pauthenet, R. & Durif, A. (1970). *Structure aux rayons X, neutrons et propriétés magnétiques des orthovanadates de nickel et de cobalt. Acta Cryst.* B**26**, 2036–2046.

Gukasov, A. & Brown, P. J. (2010). *Determination of atomic site susceptibility tensors from neutron diffraction data on polycrystalline samples. J. Phys. Condens. Matter*, **22**, 502201.

Hansen, T. C., Henry, P. F., Fischer, H. E., Torregrossa, J. & Convert, P. (2008). *The D20 instrument at the ILL: a versatile high-intensity two-axis neutron diffractometer. Meas. Sci. Technol.* **19**, 034001.

Herklotz, M., Scheiba, F., Hinterstein, M., Nikolowski, K., Knapp, M., Dippel, A.-C., Giebeler, L., Eckert, J. & Ehrenberg, H. (2013). *Advances in in situ powder diffraction of battery materials: a case study of the new beamline P02.1 at DESY, Hamburg. J. Appl. Cryst.* **46**, 1117–1127.

Hinterstein, M. (2011). *Mikrostrukturanalyse von Piezokeramiken mit Hilfe von Synchrotron- und Neutronenstrahlung*. Goettingen: Sierke Verlag.

Hinterstein, M., Hoelzel, M., Rouquette, J., Haines, J., Glaum, J., Kungl, H. & Hoffman, M. (2015). *Interplay of strain mechanisms in morphotropic piezoceramics. Acta Mater.* **94**, 319–327.

Hinterstein, M., Knapp, M., Hölzel, M., Jo, W., Cervellino, A., Ehrenberg, H. & Fuess, H. (2010). *Field-induced phase transition in* $Bi_{1/2}Na_{1/2}TiO_3$*-based lead-free piezoelectric ceramics. J. Appl. Cryst.* **43**, 1314–1321.

Hinterstein, M., Rouquette, J., Haines, J., Papet, P., Glaum, J., Knapp, M., Eckert, J. & Hoffman, M. (2014). *Structural contribution to the ferroelectric fatigue in lead zirconate titanate ceramics. Phys. Rev. B*, **90**, 094113.

Hinterstein, M., Rouquette, J., Haines, J., Papet, Ph., Knapp, M., Glaum, J. & Fuess, H. (2011). *Structural description of the macroscopic piezo- and ferroelectric properties of lead zirconate titanate. Phys. Rev. Lett.* **107**, 077602.

Hinterstein, M., Schmitt, L. A., Hoelzel, M., Jo, W., Rödel, J., Kleebe, H.-J. & Hoffman, M. (2015). *Cyclic electric field response of morphotropic* $Bi_{1/2}Na_{1/2}TiO_3$*-*$BaTiO_3$ *piezoceramics. Appl. Phys. Lett.* **106**, 222904.

Hirota, K., Wakimoto, S. & Cox, D. E. (2006). *Neutron and X-ray scattering studies of relaxors. J. Phys. Soc. Jpn*, **75**, 111006.

Hodeau, J. L., Bordet, P., Anne, M., Prat, A., Fitch, A. N., Dooryheé, E., Vaughan, G. & Freund, A. (1998). *Nine-crystal multianalyzer stage for high-resolution powder diffraction between 6 keV and 40 keV. Proc. SPIE*, **3448**, 353–361.

Hoelzel, M., Senyshyn, A., Gilles, R., Boysen, H. & Fuess, H. (2007). *Scientific review: the structure powder diffractometer SPODI. Neutron News*, **18**, 23–26.

Hoelzel, M., Senyshyn, A., Juenke, N., Boysen, H., Schmahl, W. & Fuess, H. (2012). *High-resolution neutron powder diffractometer SPODI at research reactor FRM II. Nucl. Instrum. Methods Phys. Res. A*, **667**, 32–37.

Hoffmann, M. J., Hammer, M., Endriss, A. & Lupascu, D. C. (2001). *Correlation between microstructure, strain behavior, and acoustic emission of soft PZT ceramics. Acta Mater.* **49**, 1301–1310.

Jin, Y. M., Wang, Y. U., Khachaturyan, A. G., Li, J. E. & Viehland, D. (2003). *Conformal miniaturization of domains with low domain-wall energy: monoclinic ferroelectric states near the morphotropic phase boundaries. Phys. Rev. Lett.* **91**, 197601.

Johnsen, R. E. & Norby, P. (2013). *Capillary-based micro-battery cell for in situ X-ray powder diffraction studies of working batteries: a study of the initial intercalation and deintercalation of lithium into graphite. J. Appl. Cryst.* **46**, 1537–1543.

Johnson, I., Bergamaschi, A., Billich, H., Cartier, S., Dinapoli, R., Greiffenberg, D., Guizar-Sicairos, M., Henrich, B., Jungmann, J., Mezza, D., Mozzanica, A., Schmitt, B., Shi, X. & Tinti, G. (2014). *Eiger: a single-photon counting X-ray detector. J. Instrum.* **9**, C05032.

Jones, J. L. (2007). *The use of diffraction in the characterization of piezoelectric materials. J. Electroceram.* **19**, 69–81.

Jones, J., Hoffman, M., Daniels, J. E. & Studer, A. J. (2006). *Direct measurement of the domain switching contribution to the dynamic piezoelectric response in ferroelectric ceramics. Appl. Phys. Lett.* **89**, 092901.

Jones, J. L., Pramanick, A., Nino, J. C., Maziar Motahari, S., Üstündag, E., Daymond, M. R. & Oliver, E. C. (2007). *Time-resolved and orientation-dependent electric-field-induced strains in lead zirconate titanate ceramics. Appl. Phys. Lett.* **90**, 172909.

Kenzelmann, M., Harris, A. B., Aharony, A., Entin-Wohlman, O., Yildirim, T., Huang, Q., Park, S., Lawes, G., Broholm, C., Rogado, N., Cava, R. J., Kim, K. H., Jorge, G. & Ramirez, A. P. (2006). *Field dependence of magnetic ordering in kagomé-staircase compound. Phys. Rev. B*, **74**, 014429.

Kimura, H., Kamada, Y., Noda, Y., Wakimoto, S., Kaneko, K., Metoki, N., Kakurai, K. & Kohn, K. (2007). *Field-induced dielectric and magnetic phase transitions in multiferroic compounds of* RMn_2O_5 *(R = Er, Ho). J. Korean Phys. Soc.* **51**, 870–873.

Kimura, H., Noda, Y. & Kohn, K. (2009). *Spin-driven ferroelectricity in the multiferroic compounds of* RMn_2O_5*. J. Magn. Magn. Mater.* **321**, 854–857.

Kimura, T., Goto, T., Shintani, H., Ishizaka, K., Arima, T. & Tokura, Y. (2003). *Magnetic control of ferroelectric polarization. Nature*, **426**, 55–58.

Köhli, M., Allmendinger, F., Häussler, W., Schröder, T., Klein, M., Meven, M. & Schmidt, U. (2016). *Efficiency and spatial resolution of the CASCADE thermal neutron detector. Nucl. Instrum. Methods Phys. Res. A*, **828**, 242–249.

Koyama, K., Watanabe, K., Tegus, O., Brück, E., Buschow, K. H. J. & de Boer, F. R. (2013). *X-ray powder diffraction studies on* $MnFeP_{0.78}Ge_{0.22}$ *in high magnetic fields. J. Low Temp. Phys.* **170**, 279–284.

Kraft, P., Bergamaschi, A., Bronnimann, Ch., Dinapoli, R., Eikenberry, E. F., Graafsma, H., Henrich, B., Johnson, I., Kobas, M., Mozzanica, A., Schleputz, C. M. & Schmitt, B. (2009). *Characterization and calibration of PILATUS detectors. IEEE Trans. Nucl. Sci.* **56**, 758–764.

Lee, P. L., Shu, D., Ramanathan, M., Preissner, C., Wang, J., Beno, M. A., Von Dreele, R. B., Ribaud, L., Kurtz, C., Antao, S. M., Jiao, X. & Toby, B. H. (2008). *A twelve-analyzer detector system for high-resolution powder diffraction. J. Synchrotron Rad.* **15**, 427–432.

Levin, I., Reaney, I. M., Anton, E.-M., Jo, W., Rödel, J., Pokorny, J., Schmitt, L. A., Kleebe, H.-J., Hinterstein, M. & Jones, J. L. (2013). *Local structure, pseudosymmetry, and phase transitions in $Na_{1/2}Bi_{1/2}TiO_3$–$K_{1/2}Bi_{1/2}TiO_3$ ceramics. Phys. Rev. B*, **87**, 024113.

Liss, K. D., Hunter, B., Hagen, M., Noakes, T. & Kennedy, S. (2006). *Echidna – the new high-resolution powder diffractometer being built at OPAL. Physica B*, **385–386**, 1010–1012.

Liu, L., Knapp, M., Ehrenberg, H., Fang, L., Fan, H., Schmitt, L. A., Fuess, H., Hoelzel, M., Dammak, H., Thi, M. P. & Hinterstein, M. (2017). *Average vs. local structure and composition-property phase diagram of $K_{0.5}Na_{0.5}NbO_3$–$Bi_{1/2}Na_{1/2}TiO_3$ system. J. Eur. Ceram. Soc.* **37**, 1387–1399.

Mikhailova, D., Schwarz, B., Senyshyn, A., Bell, A. M. T., Skourski, Y., Ehrenberg, H., Tsirlin, A. A., Agrestini, S., Rotter, M., Reichel, P., Chen, J. M., Hu, Z., Li, Z. M., Li, Z. F. & Tjeng, L. H. (2012). *Magnetic properties and crystal structure of SrCoIrO and SrNiIrO. Phys. Rev. B*, **86**, 134409.

Mitsui, Y., Koyama, K. & Watanabe, K. (2009). *X-ray diffraction measurements in high magnetic fields and at high temperatures. Sci. Technol. Adv. Mater.* **10**, 014612.

Mittemeijer, E. J. & Welzel, U. (2012). Editors. *Modern Diffraction Methods*. Weinheim: Wiley-VCH.

Morcrette, M., Rozier, P., Dupont, L., Mugnier, E., Sannier, L., Galy, J. & Tarascon, J.-M. (2003). *A reversible copper extrusion–insertion electrode for rechargeable Li batteries. Nat. Mater.* **2**, 755–761.

Mozzanica, A., Bergamaschi, A., Cartier, S., Dinapoli, R., Greiffenberg, D., Johnson, I., Jungmann, J., Maliakal, D., Mezza, D., Ruder, C., Schaedler, L., Schmitt, B., Shi, X. & Tinti, G. (2014). *Prototype characterization of the JUNGFRAU pixel detector for SwissFEL. J. Instrum.* **9**, C05010.

Nikolowski, K., Baehtz, C., Bramnik, N. N. & Ehrenberg, H. (2005). *A Swagelok-type in situ cell for battery investigations using synchrotron radiation. J. Appl. Cryst.* **38**, 851–853.

Noheda, B., Gonzalo, J. A., Cross, L. E., Guo, R., Park, S. E., Cox, D. E. & Shirane, G. (2000). *Tetragonal-to-monoclinic phase transition in a ferroelectric perovskite: the structure of $PbZr_{0.52}Ti_{0.48}O_3$. Phys. Rev. B*, **61**, 8687–8695.

Ohzuku, T., Ueda, A. & Nagayama, M. (1993). *Electrochemistry and structural chemistry of $LiNiO_2$ (R3m) for 4 volt secondary lithium cells. J. Electrochem. Soc.* **140**, 1862–1870.

Oswald, S., Nikolowski, K. & Ehrenberg, H. (2009). *Quasi in situ XPS investigations on intercalation mechanisms in Li-ion battery materials. Anal. Bioanal. Chem.* **393**, 1871–1877.

Patterson, B. D., Brönnimann, C., Maden, D., Gozzo, F., Groso, A., Schmitt, B., Stampanoni, M. & Willmott, P. R. (2005). *The materials science beamline at the Swiss Light Source. Nucl. Instrum. Methods Phys. Res. B*, **238**, 224–228.

Pecharsky, V. K., Mudryk, Ya. & Gschneidner, K. A. Jr (2007). *In-situ powder diffraction in high magnetic fields. Z. Kristallogr. Suppl.* **26**, 139–145.

Peral, I., McKinlay, J., Knapp, M. & Ferrer, S. (2011). *Design and construction of multicrystal analyser detectors using Rowland circles: application to MAD26 at ALBA. J. Synchrotron Rad.* **18**, 842–850.

Poikela, T., Plosila, J., Westerlund, T., Campbell, M., Gaspari, M. D., Llopart, X., Gromov, V., Kluit, R., van Beuzekom, M., Zappon, F., Zivkovic, V., Brezina, C., Desch, K., Fu, Y. & Kruth, A. (2014). *Timepix3: a 65k channel hybrid pixel readout chip with simultaneous ToA/ToT and sparse readout. J. Instrum.* **9**, C05013.

Poizot, P., Laruelle, S., Grugeon, S., Dupont, L. & Tarascon, J.-M. (2000). *Nano-sized transition-metal oxides as negative-electrode materials for lithium-ion batteries. Nature*, **407**, 496–499.

Pramanick, A., Prewitt, A. D., Cottrell, M. A., Lee, W., Studer, A. J., An, K., Hubbard, C. R. & Jones, J. L. (2010). *In situ neutron diffraction studies of a commercial, soft lead zirconate titanate ceramic: response to electric fields and mechanical stress. Appl. Phys. A*, **99**, 557–564.

Prokhnenko, O., Stein, W.-D., Bleif, H.-J., Fromme, M., Bartkowiak, M. & Wilpert, T. (2015). *Time-of-flight extreme environment diffractometer at the Helmholtz-Zentrum Berlin. Rev. Sci. Instrum.* **86**, 033102.

Radaelli, P. G. & Chapon, L. C. (2008). *A neutron diffraction study of RMn_2O_5 multiferroics. J. Phys. Condens. Matter*, **20**, 434213.

Repper, J., Keller, T., Hofmann, M., Krempaszky, C., Werner, E. & Petry, W. (2009). *Neutron Larmor diffraction for the determination of absolute lattice spacing Adv. X-ray Anal.* **52**, 201–208.

Schmitt, B., Broennimann, C., Eikenberry, E. F., Gozzo, F., Hoermann, C., Horisberger, R. & Patterson, B. (2003). *Mythen detector system. Nucl. Instrum. Methods Phys. Res. A*, **501**, 267–272.

Schmitt, L. A., Hinterstein, M., Kleebe, H.-J. & Fuess, H. (2010). *Comparative study of two lead-free piezoceramics using diffraction techniques. J. Appl. Cryst.* **43**, 805–810.

Schmitt, L. A., Schönau, K. A., Theissmann, R., Fuess, H., Kungl, H. & Hoffmann, M. J. (2007). *Composition dependence of the domain configuration and size in $Pb[Zr_{1-x}Ti_x]O_3$ ceramics. J. Appl. Phys.* **101**, 074107.

Schneider-Muntau, H.-J., Gavrilin, A. V. & Swenson, C. A. (2006). *Magnet technology beyond 50 T. IEEE Trans. Appl. Supercond.* **16**, 926–933.

Schönau, K. A., Knapp, M., Kungl, H., Hoffmann, M. J. & Fuess, H. (2007). *In situ synchrotron diffraction investigation of morphotropic $Pb[Zr_{1-x}Ti_x]O_3$ under an applied electric field. Phys. Rev. B*, **76**, 144112.

Schönau, K. A., Schmitt, L. A., Knapp, M., Fuess, H., Eichel, R., Kungl, H. & Hoffmann, M. J. (2007). *Nanodomain structure of $Pb[Zr_{1-x}Ti_x]O_3$ at its morphotropic phase boundary: investigations from local to average structure. Phys. Rev. B*, **75**, 184117.

Sears, V. F. (1992). *Neutron scattering lengths and cross sections. Neutron News*, **3**, 26–37.

Senyshyn, A., Dolotko, O., Mühlbauer, M. J., Nikolowski, K., Fuess, H. & Ehrenberg, H. (2013). *Lithium intercalation into graphitic carbons revisited: experimental evidence for twisted bilayer behavior. J. Electrochem. Soc.* **160**, A3198–A3205.

Senyshyn, A., Mühlbauer, M. J., Dolotko, O., Hofmann, M. & Ehrenberg, H. (2015). *Homogeneity of lithium distribution in cylinder-type Li-ion batteries. Sci. Rep.* **5**, 18380.

Senyshyn, A., Mühlbauer, M. J., Nikolowski, K., Pirling, T. & Ehrenberg, H. (2012). *'In-operando' neutron scattering studies on Li-ion batteries. J. Power Sources*, **203**, 126–129.

Shirane, G. (1959). *A note on the magnetic intensities of powder neutron diffraction. Acta Cryst.* **12**, 282–285.

Stefanescu, I., Christensen, M., Fenske, J., Hall-Wilton, R., Henry, P. F., Kirstein, O., Müller, M., Nowak, G., Pooley, D., Raspino, D., Rhodes, N., Šaroun, J., Schefer, J., Schooneveld, E., Sykora, J. & Schweika, W. (2017). *Neutron detectors for the ESS diffractometers. J. Instrum.* **12**, P01019.

Studer, A. J., Hagen, M. E. & Noakes, T. J. (2006). *Wombat: the high-intensity powder diffractometer at the OPAL reactor. Physica B*, **385–386**, 1013–1015.

Suard, E. & Hewat, A. (2001). *The super-D2B project at the ILL. Neutron News*, **12**, 30–33.

Toraya, H., Hibino, H. & Ohsumi, K. (1996). *A new powder diffractometer for synchrotron radiation with a multiple-detector system. J. Synchrotron Rad.* **3**, 75–83.

Weirich, T. E., Lábár, J. L. & Zuo, X. (2006). Editors. *Electron Crystallography. Nato Science Series, Series II: Mathematics, Physics and Chemistry*, Vol. 211. Heidelberg: Springer-Verlag.

Whittingham, M. S. (1976). *Electrical energy storage and intercalation chemistry. Science*, **192**, 1126–1127.

Wilson, N. R., Petrenko, O. A. & Chapon, L. C. (2007). *Magnetic phases in the kagomé staircase compound studied using powder neutron diffraction. Phys. Rev. B*, **75**, 094432.

Yoo, C.-S., Wei, H., Chen, J.-Y., Shen, G., Chow, P. & Xiao, Y. (2011). *Time- and angle-resolved X-ray diffraction to probe structural and chemical evolution during Al-Ni intermetallic reactions. Rev. Sci. Instrum.* **82**, 113901.

Yusuf, S. M., Jain, A. & Keller, L. (2013). *Field induced incommensurate-to-commensurate magnetic phase transition in $Ca_3Co_{1.8}Fe_{0.2}O_6$: a neutron diffraction study. J. Phys. Condens. Matter*, **25**, 146001.

Zhang, S. T., Kounga, A. B., Aulbach, E., Ehrenberg, H. & Rödel, J. (2007). *Giant strain in lead-free piezoceramics $Bi_{0.5}Na_{0.5}TiO_3$–$BaTiO_3$–$K_{0.5}Na_{0.5}NbO_3$ system. Appl. Phys. Lett.* **91**, 112906.